HAL
open science

Faulting and volcanism in the axial valley of the slow-spreading center of the Mariana back arc basin from Wadatsumi side-scan sonar images

Anne Deschamps, Toshiya Fujiwara, Miho Asada, Laurent Montési, Pascal Gente

To cite this version:

Anne Deschamps, Toshiya Fujiwara, Miho Asada, Laurent Montési, Pascal Gente. Faulting and volcanism in the axial valley of the slow-spreading center of the Mariana back arc basin from Wadatsumi side-scan sonar images. Geochemistry, Geophysics, Geosystems, 2005, 6 (5), pp.Q05006. 10.1029/2004GC000881 . hal-00113699

HAL Id: hal-00113699

https://hal.science/hal-00113699

Submitted on 15 Feb 2011

HAL is a multi-disciplinary open access archive for the deposit and dissemination of scientific research documents, whether they are published or not. The documents may come from teaching and research institutions in France or abroad, or from public or private research centers.

L'archive ouverte pluridisciplinaire **HAL**, est destinée au dépôt et à la diffusion de documents scientifiques de niveau recherche, publiés ou non, émanant des établissements d'enseignement et de recherche français ou étrangers, des laboratoires publics ou privés.

Geochemistry Geophysics Geosystems G3
AN ELECTRONIC JOURNAL OF THE EARTH SCIENCES
Published by AGU and the Geochemical Society

Article
Volume 6, Number 5
13 May 2005
Q05006, doi:10.1029/2004GC000881
ISSN: 1525-2027

Faulting and volcanism in the axial valley of the slow-spreading center of the Mariana back arc basin from Wadatsumi side-scan sonar images

Anne Deschamps
Department of Geology and Geophysics, Woods Hole Oceanographic Institution, 360 Woods Hole Road, Clark South 272C, MS 24, Woods Hole, Massachusetts 02543, USA (adeschamps@whoi.edu)

Toshiya Fujiwara
Deep-Sea Research Department, Japan Marine Science and Technology Center, 2-15 Natsushima-cho, Yokosuka, Japan

Miho Asada
Department of Ocean Floor Geoscience, Ocean Research Institute, University of Tokyo, Tokyo, Japan

Laurent Montési
Department of Geology and Geophysics, Woods Hole Oceanographic Institution, 360 Woods Hole Road, Clark South 272C, MS 24, Woods Hole, Massachusetts 02543, USA

Pascal Gente
UMR 6538, "Domaines Océaniques," CNRS, Institut Université Européen de la Mer, Plouzané, France

[1] We analyzed in detail the geology of the median valley floor of the Mariana Basin slow-spreading ridge using sea surface geophysical data and a high-resolution deep-tow side-scan sonar survey over one spreading segment. Analysis of surface magnetic data indicates highly asymmetric accretion, with the half-spreading rate on the western side of the basin being two to three times larger than on the eastern side. Surface magnetic and reflectivity data together suggest that asymmetric spreading is accomplished through eastward ridge jumps of ~10 km of amplitude. Deep-tow backscatter data indicate along-axis variations of the volcanic processes with the emplacement of smooth and hummocky flows at the segment center and end, respectively. This variation likely relates to changes in the effusion rate due to the deepening or even disappearance of the magma chamber toward the segment end. Concerning tectonic processes, we find a power law distribution of the fractures, with an exponent of 1.74. This suggests that within the inner valley floor, fracture growth prevails over fracture nucleation and coalescence and that fractures accommodate less than 8% of the strain. According to our calculation based on a ratio of 0.02 to 0.03 between the vertical displacement and the length of faults, the amount of tectonic strain accommodated in the inner valley floor would consistently be ~1.1–3.4%. Data also show two distinct sets of fractures. One trend is parallel to the rift direction at the segment center (~N160°E) and perpendicular to the plate separation direction. Another set trends ~17° oblique to this direction (~N175°E) and is located over the eastern part of the valley, in the vicinity of a major bounding fault also trending ~N175°E, that is, obliquely to the direction of plate motion. We modeled the stress field near a major fault that is oblique to the regional stress field associated with plate separation using a three-dimensional boundary element approach. We found that the orientation of the predicted fissuring near the oblique fault is locally rotated by ~15° due to a flexure of the bending plate close to this fault.

Components: 13,893 words, 23 figures.

Keywords: back arc; deep tow; faulting; ridge; side-scan sonar; volcanism.

Index Terms: 3035 Marine Geology and Geophysics: Midocean ridge processes; 8010 Structural Geology: Fractures and faults; 8414 Volcanology: Eruption mechanisms and flow emplacement.

Copyright 2005 by the American Geophysical Union

Received 17 November 2004; **Revised** 1 March 2005; **Accepted** 22 March 2005; **Published** 13 May 2005.

Deschamps, A., T. Fujiwara, M. Asada, L. Montési, and P. Gente (2005), Faulting and volcanism in the axial valley of the slow-spreading center of the Mariana back arc basin from Wadatsumi side-scan sonar images, *Geochem. Geophys. Geosyst.*, *6*, Q05006, doi:10.1029/2004GC000881.

1. Introduction

[2] Mid-ocean ridge spreading segments have been extensively studied over the past decade. Geological and geophysical data show that accretion processes at slow-spreading ridges are divided into distinct spreading cells, or segments, separated by first- or second-order discontinuities [e.g., *Sempéré et al.*, 1993; *Macdonald*, 1998]. Most segments end in short, nontransform offsets the evolution of which is commonly characterized by along-axis migration and limited life span [e.g., *Carbotte et al.*, 1991; *Sempéré et al.*, 1993; *Gente et al.*, 1995]. Second-order segmentation is related to a preferential delivery of melt to segments centers, where the crust is the thickest [e.g., *Lin et al.*, 1990; *Sempéré et al.*, 1993; *Tolstoy et al.*, 1993; *Detrick et al.*, 1995; *Pariso et al.*, 1995]. Seismic studies show that these crustal thickness variations mostly affect layer 3 (mainly gabbros) [*Tolstoy et al.*, 1993; *Wolfe et al.*, 1995]. The along-axis distribution of microearthquakes shows an increase in hypocenter depths for some segments [*Kong et al.*, 1992]. These observations suggest that there are significant along-axis lithospheric variations at slow-spreading ridges, with a thinner and warmer lithosphere at segments centers, and a colder, thicker lithosphere near segment ends. How eruptive processes vary and evolve across- and along- axis remains, however, poorly constrained. Moreover, the along-axis variations of crustal thickness and thermal structure can have important effects on the kinematics and mechanisms of faulting [*Carbotte and Macdonald*, 1990; *Shaw and Lin*, 1993; *Escartin et al.*, 1997], but a more complete characterization of this process has been limited by the lack of high-resolution data over spreading segments, especially in back arc environments.

[3] This paper presents results from the analysis of Wadatsumi (SYSTEM 100D) high-resolution side-scan sonar data collected in 2003 during cruise MICRO-MAR (MICRO bathymetry on the MARiana spreading ridge) of the R/V *Kairei* along a 22-km-long section of the Mariana Basin's spreading ridge, between 16°56′N and 17°09′N. This survey was performed to image fissures, faults, volcanic vents and lava flow fields. Our objective was to assess the nature and partitioning of the faulting and volcanic processes, and their variation along and across the spreading segment. We analyzed the distribution of faults and volcanic constructions in the axial valley. We also performed three-dimensional (3-D) boundary element calculations to examine the effects of a major rift-bounding normal fault trending obliquely to the plate separation direction, on the orientation of the local stress field. We discuss intrasegment variations of the tectonic and volcanic activities implications for the deep structure of the ridge, for the stress pattern in this area, and for the asymmetry of spreading.

2. Geologic Framework

2.1. Characteristics of the Mariana Basin Slow-Spreading Ridge

[4] The Mariana Basin has been opening for the past 6 Myr [*Hussong and Uyeda*, 1982] behind the Mariana subduction zone, where the Pacific Plate subducts beneath the Philippine Sea Plate (Figure 1). Spreading processes are driven by strong extensional forces due to the combined effects of the sea-anchor force of the subducted Pacific Plate beneath the Mariana Arc and the rapid northwestward movement of the Philippine Sea Plate [*Scholz and Campos*, 1995; *Stern et al.*, 2003]. The basin extends from 12°N to 23°N and is characterized by a crescent shape. Crustal thickness varies from 4 to 7 km in its central part, with a velocity structure typical of slow-spreading ridges [e.g., *LaTraille and Hussong*, 1980; *Sinton and Hussong*, 1983]. Magmas in the central part of the basin are back arc basin basalts. They are similar to normal mid-ocean ridge basalts, but with a "subduction component" that travels with fluids extracted from the subducted slab or sediments [*Newman et al.*, 2000; *Stern et al.*, 2003].

[5] In the central part of the Mariana Basin, the full spreading rate ranges from 3 to 5 cm/yr

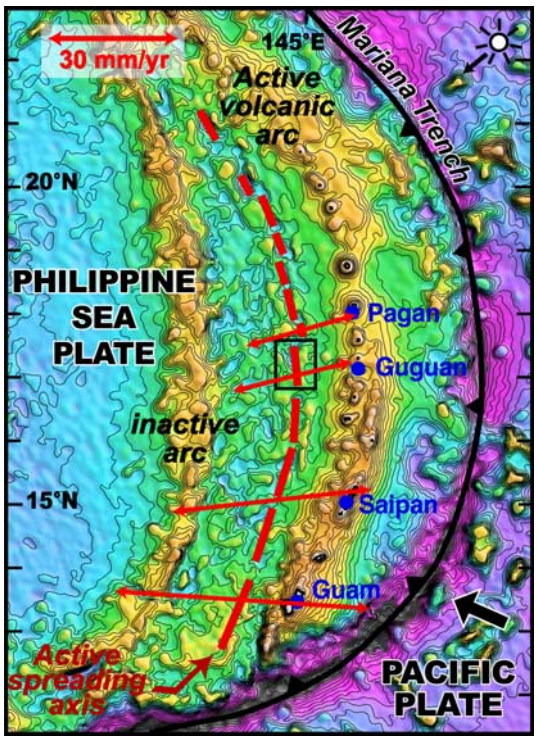

Figure 1. Geodynamic setting of the Mariana Basin, with the location of the study area (black box). Thick red lines represent the spreading axis. Red divergent arrows indicate the direction of opening calculated by *Kato et al.* [2003]. Their length is proportional to the rate of spreading.

[*Bibee et al.*, 1980; *Hussong and Uyeda*, 1982; *Seama and Fujiwara*, 1993; *Deschamps and Fujiwara*, 2003]. The spreading axis is composed of several spreading segments, each 20 to 90 km in length. Segment morphology varies from wide, deep valleys, with or without a median Axial Volcanic Ridge (AVR), to narrower, shallower and hourglass-shaped valleys. Segments with an hourglass-shaped morphology are interpreted as being more magmatically robust [e.g., *Fox et al.*, 1991; *Sempéré et al.*, 1993]. Within a single spreading segment, axial depth varies by 1–2 km between the shallow axial high at the segment center and the deeper segment ends. Each segment longer than 20 km displays along-axis variations in crustal thickness and/or upper mantle density, as demonstrated by low residual gravity anomalies at segment midpoints [*Kitada et al.*, 2002, 2004]. This is evidence that magma emplacement is focused at segment midpoints [e.g., *Lin et al.*, 1990].

[6] The Mariana Basin spreading ridge is characterized by asymmetric accretion, the half-spreading rate being two to three times larger on the western side of the ridge than on the eastern side. This asymmetry is as strong at the centers of segments as at their ends, and does not systematically correlate with an asymmetric shape of the rift valley. Segment ends typically have a half-graben shape, and at segment centers, a symmetric to slightly asymmetric graben shape characterizes the valley despite the presence of a highly asymmetric central magnetic anomaly [*Deschamps and Fujiwara*, 2003].

2.2. Morphology of the 17°N Segment

[7] The spreading segment we will discuss in this paper is ~90 km long. It is bounded by a Non-transform Discontinuity (NTD) to the south and by a Transform Fault (TF) to the north, at ~16°43′N and ~17°36′N, respectively (Figure 2). The segment trends globally south-southeast but in the vicinity of its midpoint, the rift valley trends ~N160°E. At the northern and southern ends of the segment, the rift valley floor changes in strike from ~N160°E to ~N-S. The segment is characterized by a dome-shaped morphology: the median valley floor is hourglass-shaped, narrowing and shoaling toward a bathymetric saddle (<3200 m deep) at the magmatic center (~16°58′N), and widening and deepening to >4900 m at its ends (Figures 2 and 3). The valley is ~7–15 km wide and does not contain an AVR. This segment exhibits enhanced magma supply and is likely to be characterized by a high thermal regime. Consistently, Multi Channel Seismic (MCS) data along an along-axis line displays a clear reflector that is likely related to the summit of a magma lens at ~4 km in depth beneath the median valley floor [*Taylor et al.*, 2002]. Seafloor spreading rate is 3–5 cm/yr (see references above) in a ~N73°E direction (Figure 2b) [*Kato et al.*, 2003].

[8] The rift valley is nearly symmetric at its saddle point (Figure 4a), but its walls become increasingly asymmetric toward both ends (Figure 4b). To the north, the relief on the eastern wall increases toward the RTI (Ridge Transform Intersection) and reaches ~3 km of elevation above the valley floor, while the western wall consists of a series of small-throw inward-facing normal faults (Figure 2). To the south, the western wall consists of a scarp reaching ~500 m in height at the vicinity of the NTD that bounds the segment to the south (Figure 2). The eastern wall is very poorly defined with wall-related fault scarps

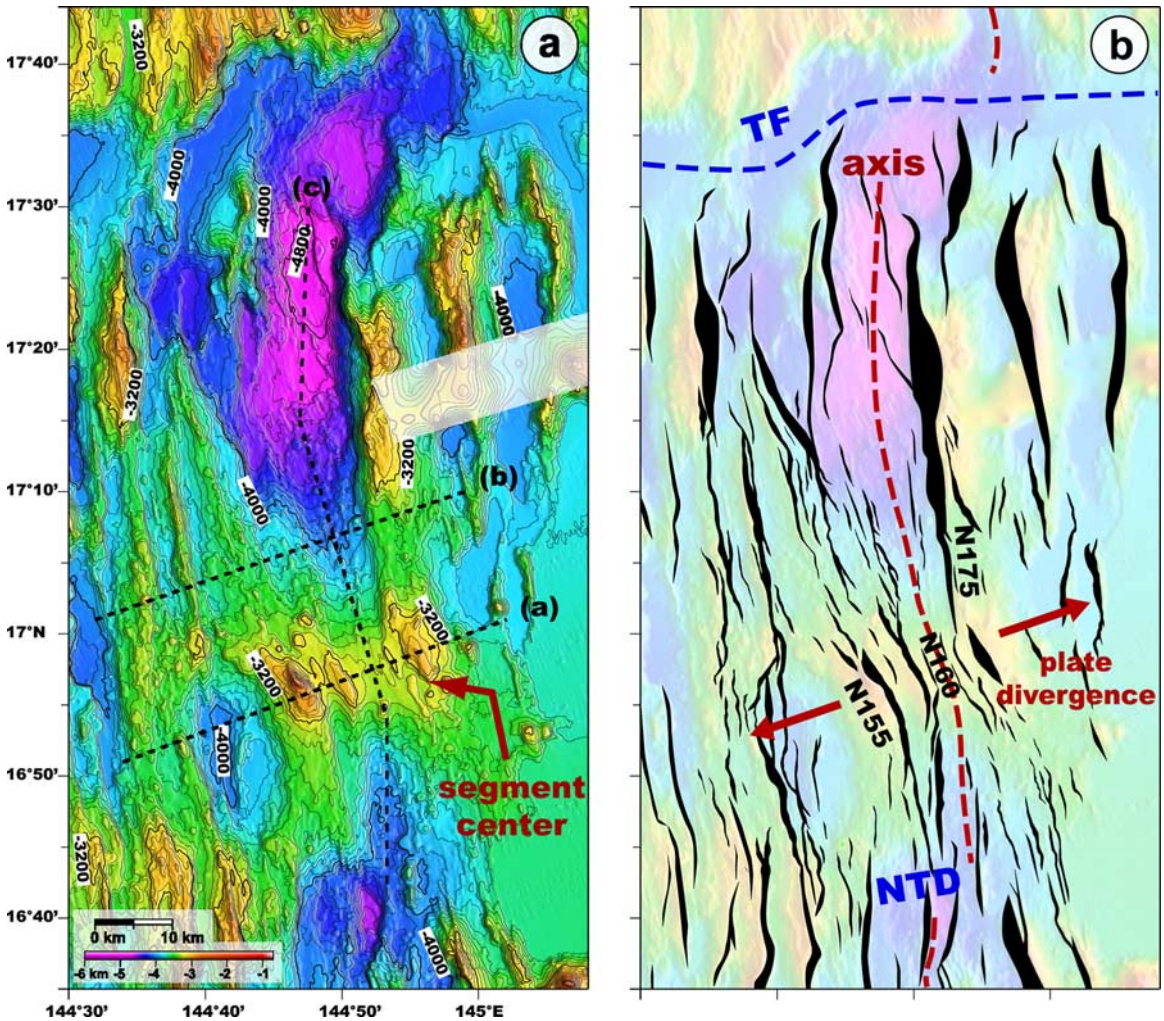

Figure 2. (a) Shaded (from E-NE) bathymetric relief of the studied spreading segment with the locations (dashed black lines a and b) of across-axis bathymetric and magnetic profiles shown in Figure 4 and the location (dashed black line c) of along-axis bathymetric and gravity profile shown in Figure 3). Isocontours every 80 m. (b) Corresponding simplified structural map with (in black) the location of the main fault scarps inferred from surface bathymetric data. The segment is bounded to the north by a transform fault (TF) and to the south by a nontransform discontinuity (NTD). Location of possible pseudo faults (PF) associated with a northward and southward propagation of the segment is indicated. Red arrows indicate the direction of opening [*Kato et al.*, 2003].

probably buried beneath constructional terrain. Such a configuration with one large fault located at the Inside Corner (IC) and several small-throw faults at the Outside Corner (OC), with a switch of polarity near the segment center, has been often observed on slow-spreading segment [e.g., *Briais et al.*, 2000].

2.3. Gravity Field

[9] Gravity data were collected during the cruise at a speed of 5–6 knots using a Bodenseewerke KSS-31 marine gravity meter. The observed free-air gravity anomaly data were merged with the satellite-derived gravity anomaly [*Smith and Sandwell*, 1997] where no shipboard gravity data are available. To examine subseafloor density variations, we calculated a Mantle Bouguer Anomaly (MBA) using the method of *Kuo and Forsyth* [1988], *Prince and Forsyth* [1988], and *Lin et al.* [1990], by subtracting from free-air gravity the predicted gravity effects of seafloor topography and a 6-km-thick model crust. Assumed densities of the crustal layer and underlying mantle are 2,700 kg/m^3 and 3,300 kg/m^3, respectively. To avoid artificial edge effects, we mirrored the grid both east-west and north-south. The MBA map of our survey area shows a large

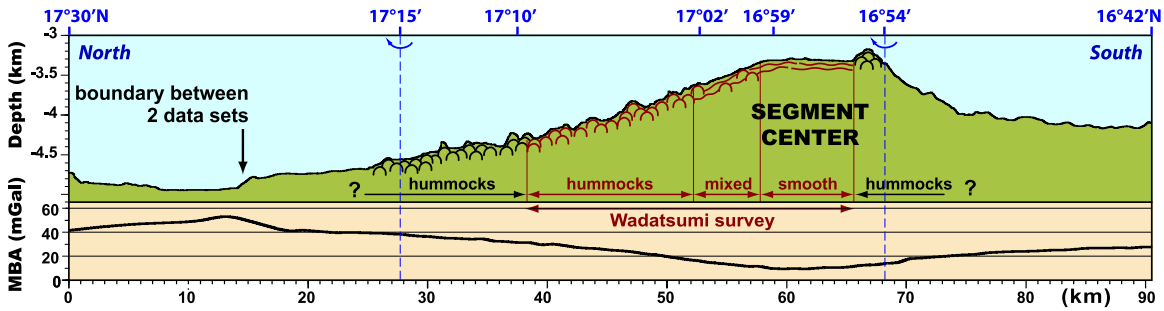

Figure 3. Bathymetric (top) and gravity (bottom) along-axis profiles. Location of the profiles in Figures 2 and 5b. The area covered during the deep-tow side-scan survey is indicated in red. Different lava morphologies observed from these data are indicated in red. Lava morphologies inferred from surface data are indicated in black. Dashed blue lines indicate the change in direction of the cross section (see Figure 2).

amplitude low centered on the segment midpoint (Figures 3 and 5b). The magnitude of this circular "bull's-eye" MBA is ~40 mGal (~1.2 mGal/km) between the center and the northern end of the segment (Figure 3). This high gradient indicates that the density structure varies rapidly along-axis, suggesting a focusing of magmatic activity toward the center of the spreading segment at ~17°N [e.g., *Lin et al.*, 1990]. Crustal thickness beneath the segment center is estimated to be ~7 km on the basis of seismic refraction data [*Takahashi et al.*, 2003]. The variation of crustal thickness between the segment center and its ends is inferred to be ~3–4 km [*Kitada et al.*, 2004], suggesting that melt supply at the end of the segment is ~50% of that at the segment center.

2.4. Surface Reflectivity Data

[10] Surface side-scan data were recorded using the hull-mounted SeaBeam 2112 (149 beams) system. High reflectivity marks the entire inner floor, with the segment midpoint having a narrower zone of high reflectivity that is clearly bounded by the first normal fault scarps found within the inner valley floor (Figure 5c). To the south, one striking feature is the presence of two parallel bands of high reflectivity. One is located along the inner valley floor and presents the same characteristics as the

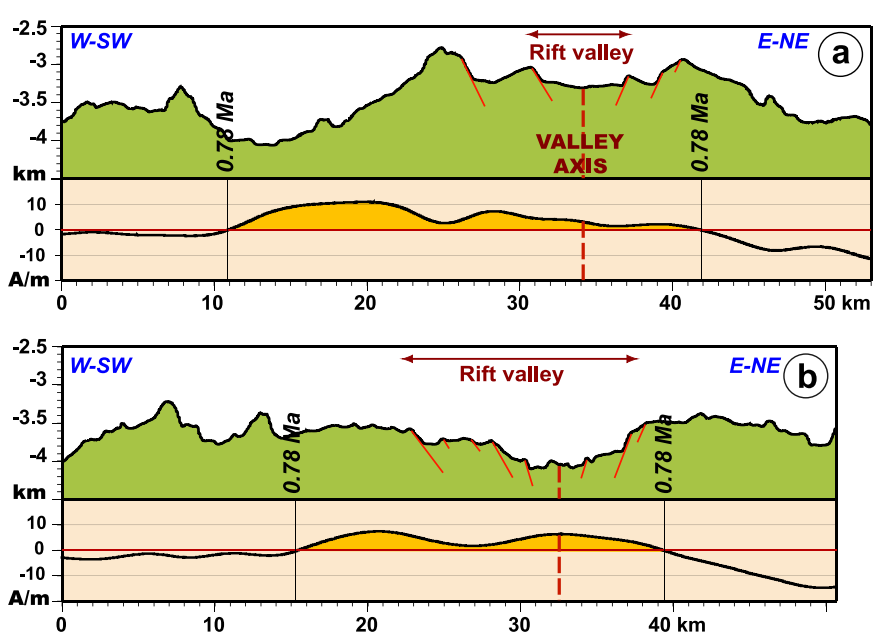

Figure 4. (a) Bathymetric and (b) magnetic across-axis profiles. Location of the profiles in Figures 2 and 5a. In the bathymetric profiles, red lines indicate the locations of rift valley major bounding faults. In the magnetic profiles, yellow areas correspond to the Brunhes anomaly. Red vertical dashed lines indicate the valley axis.

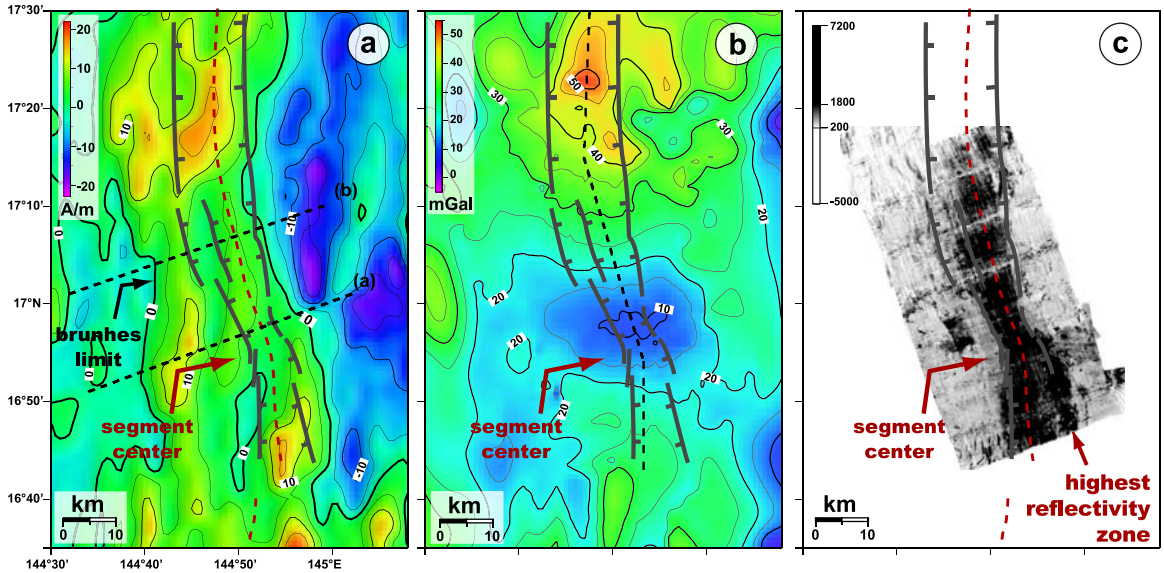

Figure 5. Maps of (a) the result of 3-D crustal magnetization calculation with the location of across-axis profiles shown in Figure 4 (contour interval is 5 A/m), (b) the mantle Bouguer anomaly map with the location of along-axis profile shown in Figure 3 (contour interval is 5 mGal), and (c) surface side-scan sonar data with the black color corresponding to the highest reflectivity. The red dashed line represents the valley axis. The location of the valley-bounding faults is indicated on every map as reference.

northern part of the segment. The second one, located east of the previous one, and associated with a series of ridges and large volcanoes identified on surface bathymetric maps, has the highest reflectivity. These two bands are separated by a narrow and less reflective area. The easternmost band of high reflectivity likely corresponds to a region of intense volcanism.

2.5. Magnetic Field Data

[11] Magnetic data over the survey area were collected in 2001 during a previous cruise [*Iwamoto et al.*, 2002]. Crustal magnetization was calculated by removing the skewness due to low magnetic latitude and correcting for effects of seafloor topography, to obtain a better estimate of source magnetization intensity, and its relationship to seafloor features. The inversion method developed by *Parker and Huestis* [1974], and extended to three dimensions by *Macdonald et al.* [1980], was used for this calculation. A uniform, 500-m-thick magnetic source layer was assumed. The magnetic signal is assumed to be primarily generated by the extrusive layer (seismic Layer 2A) at the spreading axis with little to no contribution from the lower crust due to the thermal regime [e.g., *Tivey and Tucholke*, 1998]. The direction of magnetization in the source layer was assumed to be oriented parallel to a geocentric dipole field. Bandpass filters with cosine tapers for wavelengths between 3 and 6 km and between 100 and 150 km prevent instabilities during inversion. No annihilator was added to the magnetization solution. Data coverage is limited in this area, leading to an inherent ambiguity in the zero level of the magnetization. Magnetic boundaries were therefore determined from inflection points of maximum slope on cross-axis magnetization profiles (Figures 4 and 5a). The inflection point is interpreted as the edge of the Brunhes chron on the basis of results of our modeling [e.g., *Vacquier*, 1972].

[12] A full spreading rate of 3.3 ± 0.9 cm/yr is estimated using the boundaries of the Brunhes anomaly (Figure 4). This value is consistent with the 3.2 cm/yr spreading rate estimated using geodetic data [*Kato et al.*, 2003]. A magnetization high resides west of the axial valley floor, where the surface backscatter data do not indicate any recent volcanic activity (Figures 5a and 5c). The Brunhes anomaly is not centered on the axis of the valley: at the segment midpoint, the edge of the anomaly is ~23 km (in the west) and ~8 km (in the east) from the valley axis (Figure 4). This pattern is also found at other segments of the Mariana Basin spreading ridge and is interpreted to be the result of highly asymmetric spreading [*Deschamps and Fujiwara*, 2003]. The easternmost zone of high reflectivity observed in the southern part of the segment is associated with a high magnetization.

This suggests that intense steady state volcanism occurs east of the rift valley, in the southern part of the spreading segment.

3. Deep-Tow Data Collection and Processing

[13] The "Wadatsumi" (SYSTEM 100D) deep-tow side-scan sonar from ORI (Ocean Research Institute, Univ. of Tokyo) was used to collect the high-resolution backscatter data presented in this study. It operates at a frequency of 100 kHz, at a tow altitude of ~300 m, and speed of 1.5 to 2 knots. The theoretical horizontal pixel resolutions of Wadatsumi system is 50 cm (across-track) over 100 cm (along-track) on average, such that the across- and along-track spacing of data is about 0.5 and 1 m, respectively. However, the effective spatial resolution of features is ~1 m for side-scan imagery and 4–5 m for phase-bathymetry in the seafloor terrain of the studied segment (the system produced phase-bathymetry data only on the starboard side of the sonar due to technical problems). Wadatsumi collected 1024-m-wide swaths (512 m on each side of the vehicle), each composed of 2048 pixels (or footprints) across the swath, one pixel containing a water depth and echo intensity measurement. The Wadatsumi system is very similar to the DSL-120 system (WHOI) in terms of frequency and spatial resolution (see *Scheirer et al.* [2000] for a DSL-120 description).

[14] Subbottom profiles using 4–6 kHz CHIRP profiler attached to the towfish were also collected. All measurements are corrected for towfish altitude using an internally mounted, six-component, motion-sensing unit. The entire system consists of a towfish, depressor, winch, surface electronics processing system, logging computer and printers. During this cruise, we used a 10-km-long fiber-optic cable for towing. The ship was navigated by continuous GPS. The position of the towfish was determined by an acoustic SSBL (Super Short Base Line) system with corrections based on wire length. The final position was adjusted by comparing images from overlapping tracks, as well as by comparing large-scale tectonic and volcanic features with surface bathymetric data.

[15] The survey covered a region of 22 km in length and 9 km in width, which encompassed the entire median valley floor with 10 ridge-parallel side-scan swaths. This provides us with a mosaic that covers an area of ~200 km^2 over the inner valley floor close to the 17°N segment midpoint, between 16°56′N and 17°09′N (Figures 6 and 7). The 200-m-wide nadir zone beneath the sonar vehicle contains little usable information due to the high incidence angle of the sonar pulse and to bottom detection errors.

[16] The side-scan data allow us to map fissures and small-throw faults, to differentiate between hummocky and smooth volcanic products, and fresh-looking volcanics from sediment-covered areas. Faults, fissures, grabens, smooth lava flows, hummocks and hummocky ridges have been digitized from 1/12500-scale side-scan mosaics. The images are displayed with high amplitude returns as bright pixels, and low amplitude and acoustic shadows as dark (Figure 7). Sediments cause a lower and uniform amplitude return because of acoustic penetration and attenuation in the subsurface and also make seafloor and scarps look much smoother. In the study area, sediments are only observed close to the valley walls, at a distance ranging from few hundred meters to 2.5 km. Most faults and some volcanic edifices, however, remain easily detectable because of the limited thickness of this sediment layer.

4. Magmatism on the Median Valley Floor: Observations

4.1. Constructional Terrain Inferred From Surface Bathymetric Data

[17] Surface bathymetric data show an along-axis variation in the distribution of seamounts within the median valley floor (Figures 3 and 6). In the southern part of the segment (16°43′–16°54′N), the valley floor displays numerous, almost circular, volcanic mounds, whose basal diameters range from ~300 to 1500 m, and heights range from ~20 to 200 m. In the central part of the segment, around its saddle point (16°54′N–17°01′N), only one small seamount (~500 m in diameter and ~30 m in height) and few terraces are observed. The rest of the seafloor looks smooth. In the northern part of the segment, between 17°02′N and 17°18′N, we observe ~20- to 200-m-high seamounts with diameters ranging from 300 to 1400 m (Figure 3).

[18] Several ridges, up to ~120 m high, ~1.5 km wide, and ~7 km long, are well defined. In the vicinity of the valley axis, these ridges trend

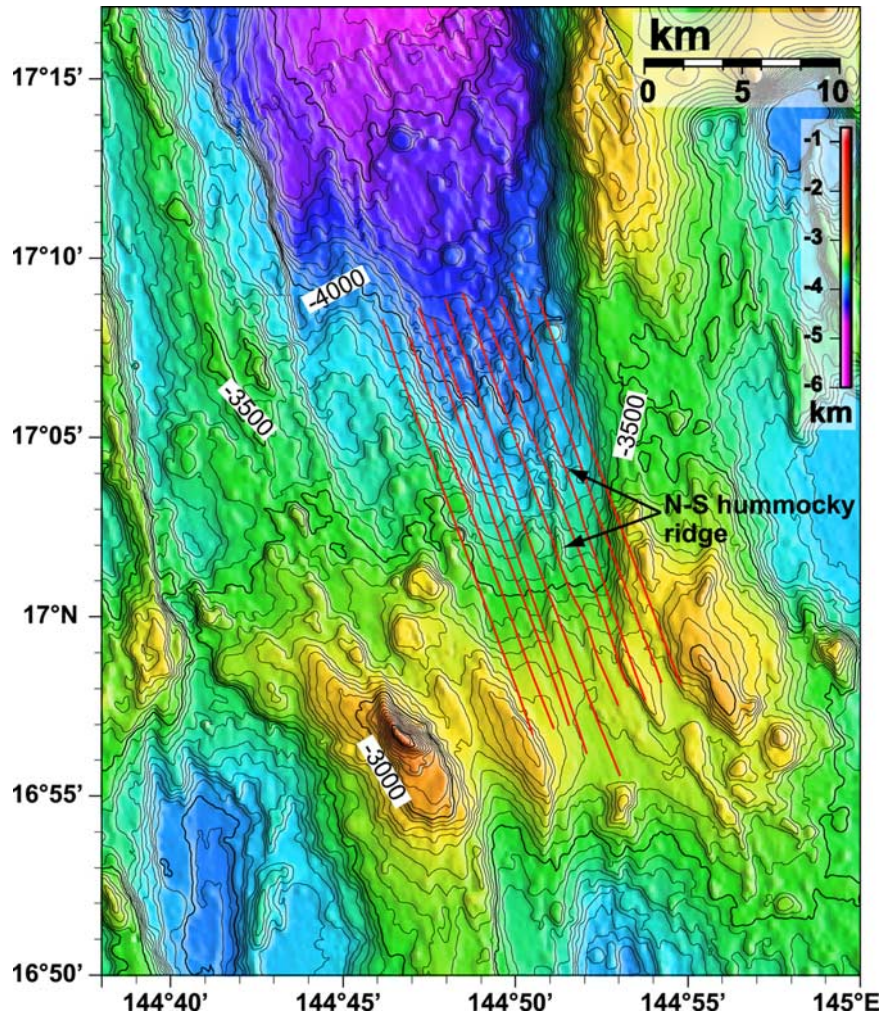

Figure 6. Wadatsumi side-scan sonar tracks shown as red lines on a bathymetric map of the studied segment (contour interval is 50 m).

~N160°E, but east of this axis, they trend ~N-S (Figure 6).

[19] In the northernmost part of the segment (17°18′N to 17°36′N close to the RTI), neither seamounts nor ridges are observed and the seafloor is relatively smooth (Figure 3). This could be related either to the absence of prominent volcanic edifices or to the presence of sediments burying most of the volcanic relief.

4.2. Volcanic Morphology Recognized From Deep-Tow Side-Scan Sonar Images

[20] From deep-tow side-scan sonar images, we can distinguish several types of constructional volcanic terrain: hummocks and hummocky ridges, large seamounts, and smooth volcanic terrain. The lack of data near the nadir of the side-scan swath leads to an underestimate of the abundance of volcanic construction; however, since the nadir affects all swaths equally, we can reliably estimate the relative abundance of hummocky and smooth lava flows within the survey area.

4.2.1. Hummocky Volcanic Texture

[21] The dominant constructional texture in the northern part of the survey area is a fine-scale hummocky volcanic terrain (Figures 7, 8, 9, and 10). It consists of a conglomeration of numerous, rounded mounds, whose diameters range from a few tens of meters to about 350 m. According to phase bathymetric data, their height is usually less than 60 m high. They have rounded summits with no craters. The hummocky terrain varies in character from steep-edged hummocks having a size often greater than 150 m in diameter,

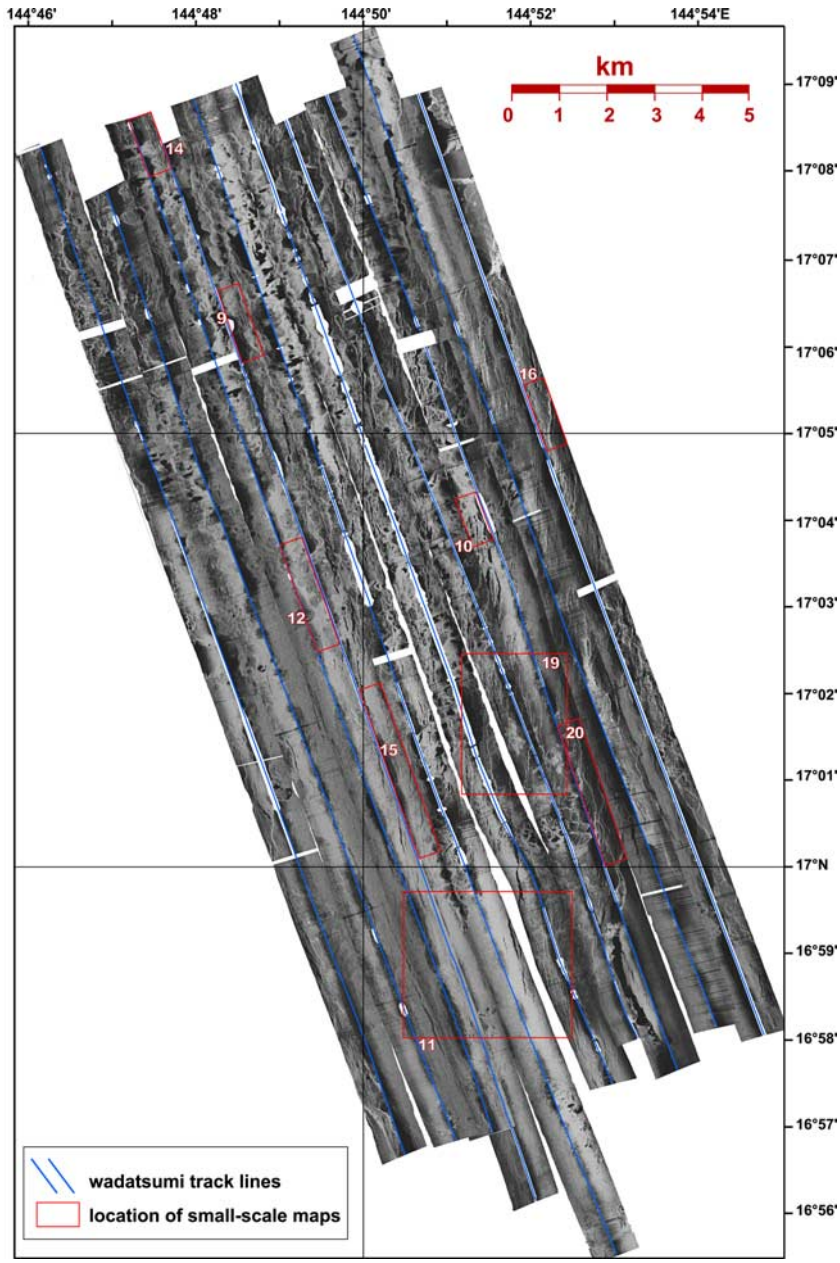

Figure 7. Side-scan mosaic of the area surveyed by Wadatsumi. Bright is reflective seafloor indicative of recent volcanic products and fault scarps facing toward the instrument. Dark is low backscatter seafloor, indicative of old volcanic constructions, sedimented areas, shadows, and scarps facing away from the instrument. Frames numbered 9 to 20 are locations of Wadatsumi small-scale mosaics shown in figures of the same number.

to dappled, lower relief areas where the diameter of each hummock is generally ~100 m and rarely exceeds 150 m.

4.2.2. Hummocky Ridges

[22] Often the hummocks are aligned and aggregated such that they form linear ridges that are up to ~7 km in length and ~1.5 km in width (~500 to ~1 km in average) (Figures 7 and 8). Frequently, hummocky domes composed of closely agglomerated hummocks are found on these ridges (Figure 9). The domes can be more than 2 km in length and 800 m in width. The lack of data between several side-scan swaths or/and nadirs prevents us from accurately measuring these large-size features. Some of the hummocky ridges trend ~N160°E, that is, parallel to the valley walls at the segment midpoint, while others, located on the eastern side of the valley,

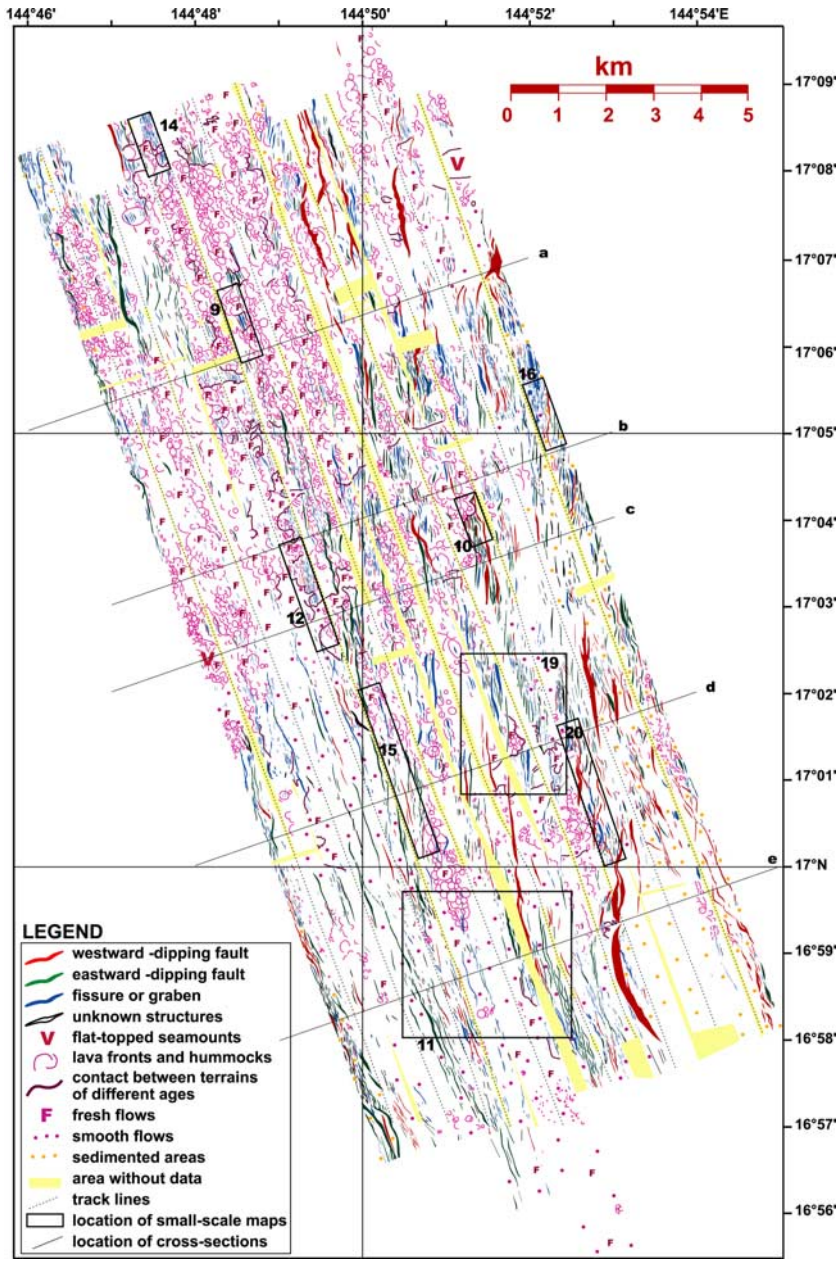

Figure 8. Geological interpretation of side-scan mosaic shown in Figure 7. Frames numbered 9 to 20 are locations of Wadatsumi small-scale mosaics shown in figures having the same number. Location of cross sections a, b, c, d, and e shown in Figure 13 is indicated in black.

trend N-S. The main ridges are visible on surface bathymetric data (Figure 6).

4.2.3. Smooth Volcanic Terrain

[23] The dominant constructional texture at the segment midpoint is a smooth, flat and highly backscattering terrain (Figures 7, 8, and 11). Between 16°55.5′N and 16°59.5′N, smooth terrain covers almost the whole valley floor. Between 16°59.5′N and 17°03′N, it covers half of the valley, with the rest being covered by hummocks. At this location, smooth terrain sometimes displays a short wavelength (~50–100 m) undulating surface (Figure 12). These very subtle bumps are likely low hummocks. Further to the north, small-size hummocks (less than 100 m in diameter) indeed become discernable among the smooth flows.

4.2.4. Flat-Topped Seamounts

[24] Only two large-size isolated seamounts with relatively smooth-textured flat tops are recognized. They are circular, 900–1300 m in diameter, and

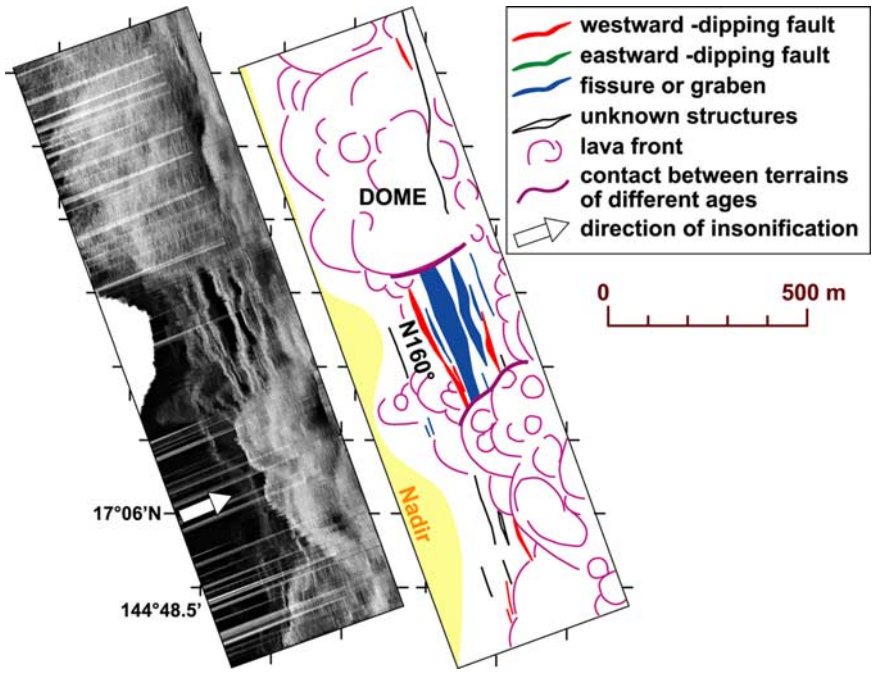

Figure 9. Small-scale side-scan mosaic with geological interpretation, showing the sharp contact between fresh hummocks and older, intensively faulted seafloor. Location in Figures 7 and 8.

220–250 m high. One volcano is located close to the western wall of the valley and is covered by sufficient sediment to make its surface smooth and poorly reflective. The other one is located at the foot of the eastern valley wall, and is characterized by steep, strongly backscattered rims (Figures 7 and 8).

4.3. Distribution of Volcanic Edifices and Relations With Small-Scale Tectonic Features

[25] We observe along- and across-axis variations in the distribution of constructional terrain: hummocks and hummocky ridges are found in the northern part of our deep-tow side-scan survey area, whereas smooth flows are observed close to the segment midpoint (see section 4.2 and Figures 7 and 8). This pattern is also visible on surface bathymetric map (section 4.1 and Figures 3 and 6). An across-axis asymmetry is also observed: the segment shows a contrast between fresh-looking volcanic terrain located mainly in the center of the valley and over its western wall, and intensely faulted seafloor covering the eastern side of the valley (Figure 13). Fresh flows cover areas that are up to 4 km wide and 12 km long along-axis. Few fresh flows are observed in the eastern part of the valley. Their dimensions never exceed 4 km in length and 1.5 km in width.

[26] Most of the fresh-looking volcanic terrain (hummocky or smooth) is cut by occasional fissures and faults. In several places, flows clearly overprint fissures and fault scarps (Figures 9, 10, 12, and 14) but are themselves cut by new fractures (Figures 7 and 10). The fresh lava observed along the western valley wall are west of the tectonized terrain and this relationship indicates that these flows flowed from west to east (Figures 8, 9, 10, 12, and 14).

5. Faulting Pattern on the Median Valley Floor

[27] The deep-tow side-scan data provide an opportunity to examine a population of small (length of 15 to 3250 m) fissures, grabens and normal faults that represent a relatively early stage of faulting (<0.25 Ma) in a slow-spreading environment. In this study, we characterize fault length, fault direction and their geographic distribution. Relatively linear, straight, and strongly backscattering features are interpreted to be fault scarps facing the sonar. They are strongly backscattering because their steeply inclined surfaces present a high angle of incidence to the sonar beam and allow minimal accumulation of sediments. Similar features with very low backscatter are viewed as shadows cast by fault scarps facing

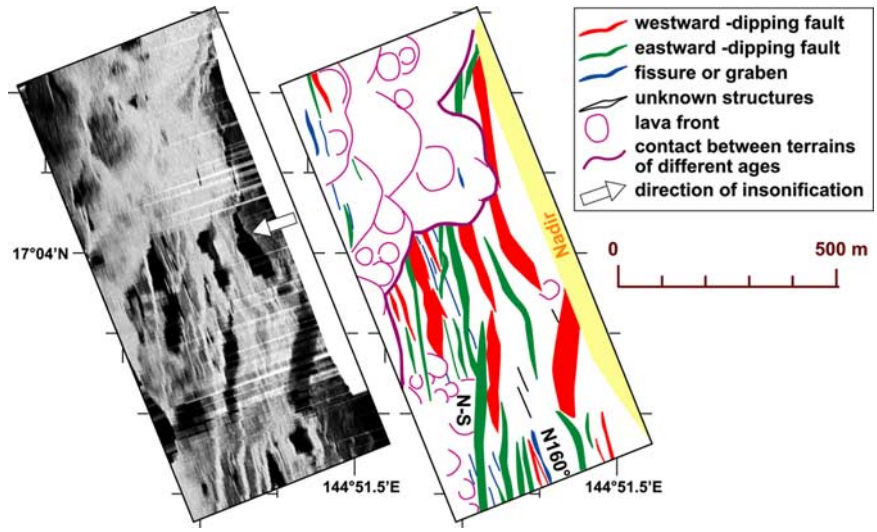

Figure 10. Small-scale side-scan mosaic with geological interpretation, showing the sharp contact between fresh hummocks and older, intensively faulted seafloor. ~N-S and ~N160°E-trending fissures and faults are present. Location in Figures 7 and 8.

away from the instrument. Relatively linear features characterized by both strongly and low backscatters on each side are considered as fissures or grabens. Distinction is sometimes ambiguous especially for small features, which lead us to perform statistical studies on the whole set of tectonic lineaments or "fractures." The lack of data near the nadir of the side-scan swath and a lack of resolution due to technical problems at some places leads to an underestimate of the abundance of tectonic features and of their length. We did not consider fractures which seem to be truncated by the nadir and swath edges for our statistical studies. We eventually mapped a total of 4124 usable tectonic lineaments (2347 fissures and grabens and 1777 normal faults) within the ~200 km^2 large study area (Figure 8). We measured their length and orientation. Uncertainties about fractures length are due to the absence of mapping of fractures or fracture tips whose size is below the resolution of data (i.e., 1 m), and also to the gap between track lines which leads to an underestimate of the length of lineaments that do not parallel the track lines despite our effort to remove such lineaments from the statistical studies. Volcanic terrain within the studied segment show various degrees of deformation from relatively recent volcanic areas with almost no fractures and/or fissures to totally dismembered zones with very intense faulting and fissuring. In general, the deformation is concentrated on the eastern side of the valley (Figures 7, 8, 11, 13, and 15). On the borders of the valley, fissures and faults cut a thin layer of sediments (Figure 16).

5.1. Fracture Length

[28] Average length of fissures is 118 m, whereas the average length of faults is 355 m (Figure 17). The average length of all fractures is 185 m. The largest faults often exhibit curvilinear traces. In detail, breached relay ramps and abandoned splays are preserved in footwall (Figures 11, 14, and 16). This reflects the along-strike linkage of coeval faults. We considered as linked faults only faults that are physically linked or separated by less than ~40 m.

[29] Cumulative size-frequency distribution of fault parameters is often used to characterize fault populations. Numerical simulations and experimental results show that exponential distribution of fracture lengths is associated with the early stages of deformation, when fracture nucleation dominates over growth and coalescence processes [e.g., *Cowie et al.*, 1993, 1995; *Bonnet et al.*, 2001; *Ackermann et al.*, 2001; *Spyropoulos et al.*, 2002]. This is the "nucleation regime." With further strain, the cracks begin to grow and to have elastic interactions between each other. This is the "growth regime." The distribution approaches a power law as described in equation (1).

$$N = A\,L^{-C}, \qquad (1)$$

where L is the fault length, N the number of fractures of length $\geq$ L, A is a constant reflecting

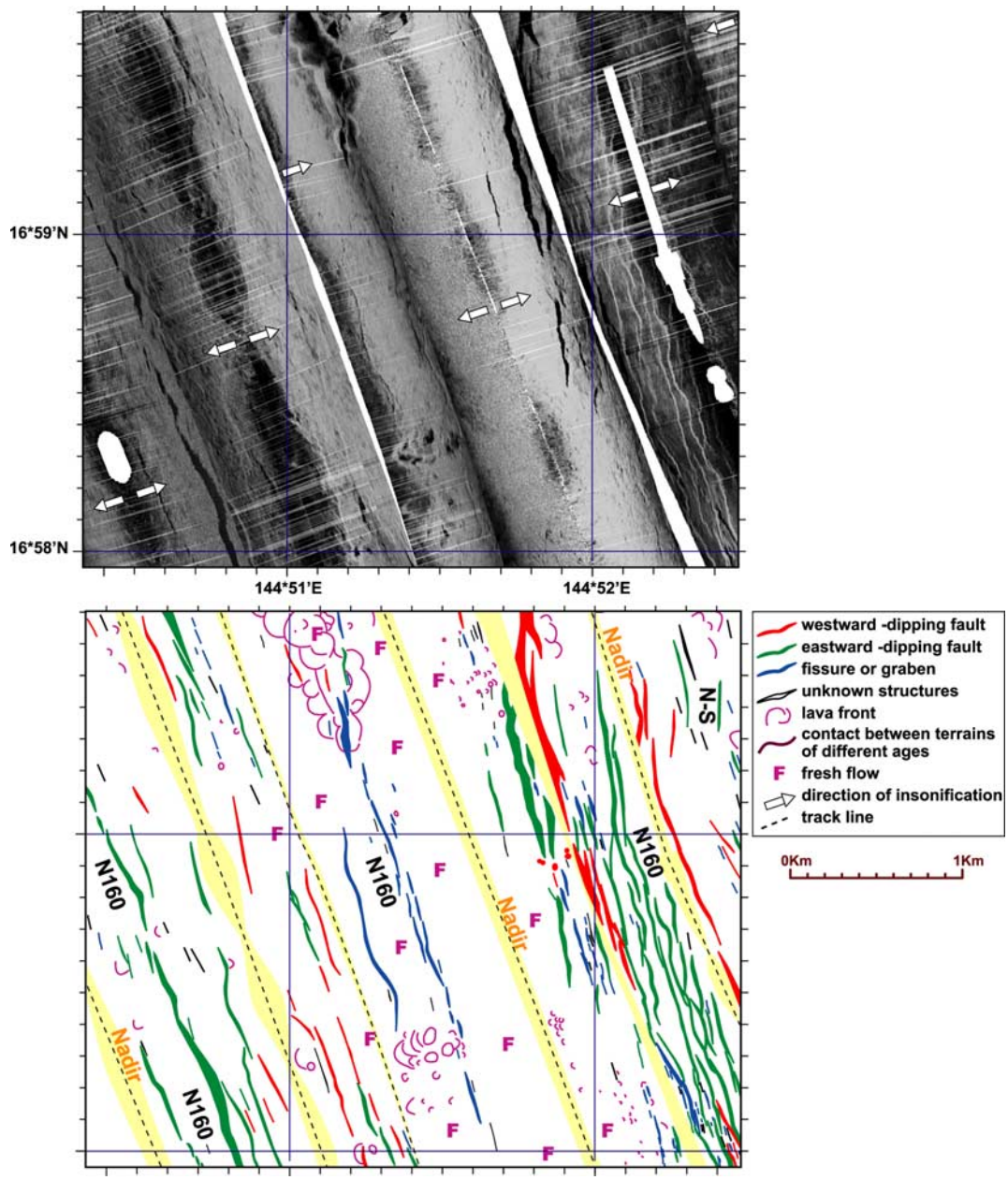

Figure 11. Small-scale side-scan mosaic with geological interpretation, showing smooth and hummocky lava flows close to the segment midpoint. Location in Figures 7 and 8.

the size of the population, and C is the power law exponent (i.e., the slope of the straight-line part of the curve in a log-log plot). A power law distribution plots as straight line in log-log space. As strain continues, more cracks coalesce to form longer cracks than there are cracks nucleating, and therefore the number of active cracks begins to decrease. The power law becomes distorted, with the largest cracks approaching an exponential distribution (2). This is the "coalescence regime." It is worth noting that there is a gradual evolution between the "growth regime" and the "coalescence regime" [e.g., *Spyropoulos et al.*, 1999]. The exponential distribution is described by the following relationship:

$$N = Be^{-\lambda L}, \tag{2}$$

where N is the number of faults with length larger than a given value of length L, B is a constant reflecting the number of faults, and λ is inverse of L, the characteristic (or mean) value of L if the population is properly characterized by an exponential distribution. An exponential distribution

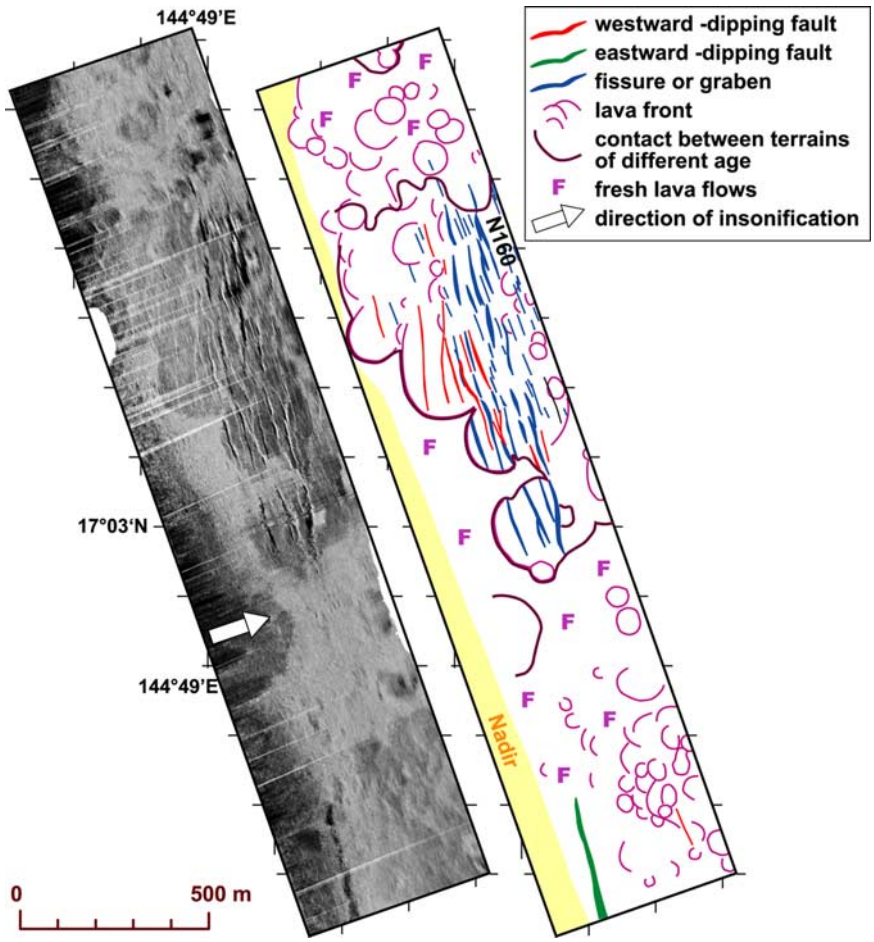

Figure 12. Small-scale side-scan mosaic with geological interpretation. There is a sharp contrast between fresh flows and fissured seafloor. Location in Figures 7 and 8.

plots as a straight line in linear-log space, λ being the slope of the best-fit line for the data. Finally, for higher strains, the cracks grow into a pattern of long arrays that are proportionally spaced according to the depth of the brittle layer. Faults then become constrained structures, having lost the freedom to grow vertically, and cannot have elastic interactions with other faults. This is the "saturation regime" where large faults have an exponential distribution [e.g., *Ackermann and Schlische*, 1997; *Spyropoulos et al.*, 1999, 2002; *Gupta and Scholz*, 2000; *Ackermann et al.*, 2001].

[30] Figure 18 shows the distribution of all (4123) fractures lengths (L), plotted on log linear and log-log scales. On log-log length versus cumulative frequency plot, the data points lie along a curve that has three distinct segments, similar to other cumulative frequency plots [e.g., *Pickering et al.*, 1995; *Schlische et al.*, 1996]. Truncation at the longest lengths results from the artificial segmentation of the traces of the longest faults. Truncation at shorter lengths reflects data censoring resulting from detection limits of the Wadatsumi to resolve fracture tips. The central linear part of the curve indicates that the whole population ($180 \leq L \leq 1250$ m) follows a fractal distribution with a power law of the form $N = 1E07.\ L^{-1.74}$. The power law exponent C is equal to 1.74. It is the slope of the straight-line part of the curve. Correlation coefficient for power law fit is 0.99.

[31] The 1.74 value of C for the whole population likely means that fractures in the study area did accommodate a relatively small amount of strain. Terrestrial studies indeed reveal that where the data show unequivocal power law behavior [e.g., *Scholz et al.*, 1993] the brittle strain is less than 8% (often less than 2%), but in the case where the distribution is clearly exponential, the strain is much higher (8–15%) [*Cowie et al.*, 1993; *Gupta and Scholz*, 2000]. A similar breakdown from a power law size distribution for increasing strain was observed in a

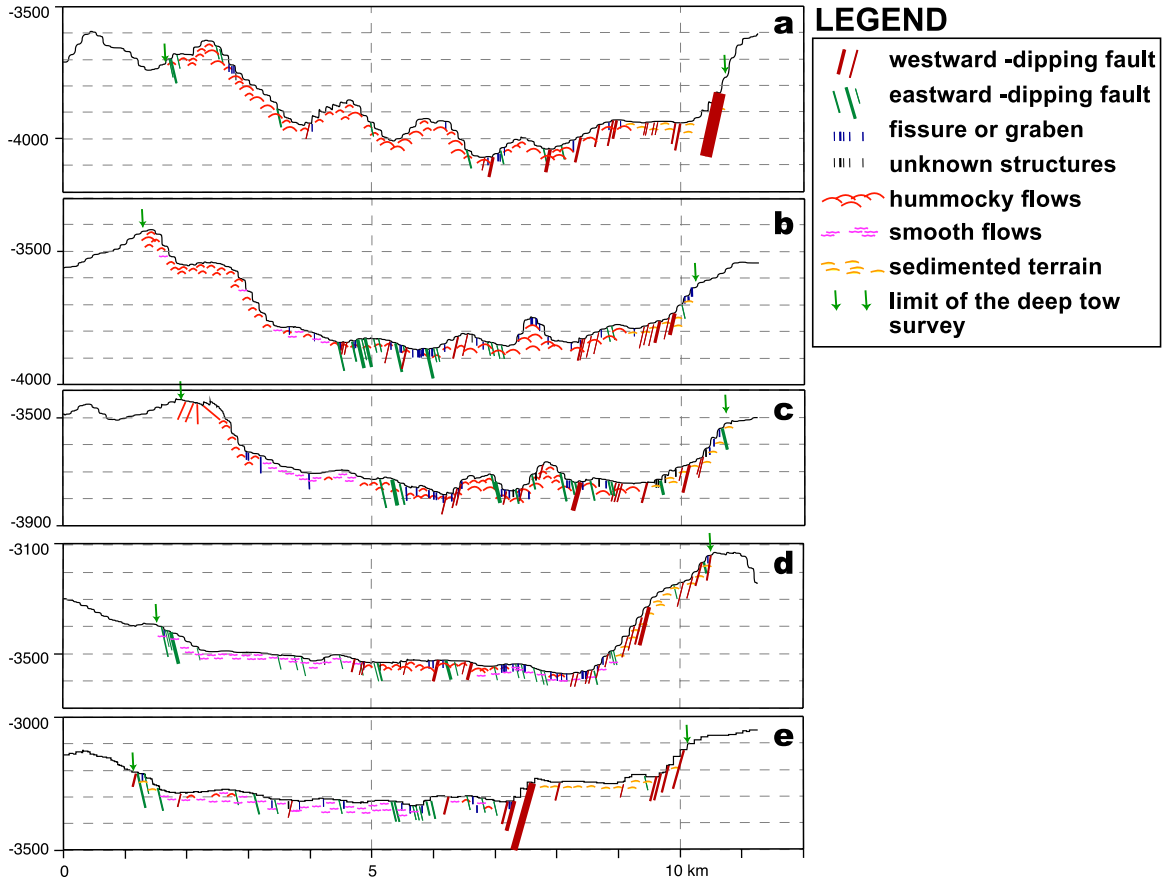

Figure 13. Bathymetric cross sections (from surface data) with geological interpretations deduced from Wadatsumi side-scan data. The seafloor is apparently more tectonized in the eastern part of the valley. Location of section in Figure 8.

numerical [*Spyropoulos et al.*, 2002] and analog [e.g., *Spyropoulos et al.*, 1999; *Ackermann et al.*, 2001] models.

[32] Calculations of the amount of strain based on a reasonable d/L ratio between the vertical displacement (d) and the length of faults (L) give consistent results. Using the mean calculated fault length of 355 m (see above), the strain value calculated on the basis of a 0.03 ratio is 1.72 to 3.4% depending on the assumed fault dip (70° to 55°). 0.03 is a reasonable value for d/L ratio because it is calculated on continental faults over more than eight orders of magnitude (see the compilation by *Schlische et al.* [1996]) and in the axial valley of the MAR [*Bohnenstiehl and Kleinrock*, 1999]. We however did also strain calculations based on a d/L ratio of 0.02 because few studies at sea show that the d/L ratio of normal faults might be lower than in continental domain [*Cowie et al.*, 1993, 1994; *Carbotte and Macdonald*, 1994; *Cowie*, 1998; *Bohnenstiehl and Kleinrock*, 2000]. In this case, the calculated strain is 1.15 to 2.2%, depending on the fault dip (70° to 55°).

[33] The value of ~1.1–3.4% for the strain accommodated in the inner valley floor is consistent with the results of *Bohnenstiehl and Kleinrock* [1999], who calculated ~1.5% of brittle deformation on the valley floor of the slow-spreading mid-Atlantic ridge at ~26°N, by a population of small fractures (150–1100 m in length) which length distribution is characterized by a power law exponent of 1.64–1.96.

[34] The nonperfect power law distribution for fractures longer than ~700 m may indicate that these fractures are approaching an exponential distribution due to linkage phenomena. We indeed observe that the longest faults are linked together (Figure 20). It could also reflect an underestimation of the longest faults of the survey area, because (1) the sonar coverage is incomplete such that some faults are artificially broken up into smaller faults where they cross nadir or are slightly offset

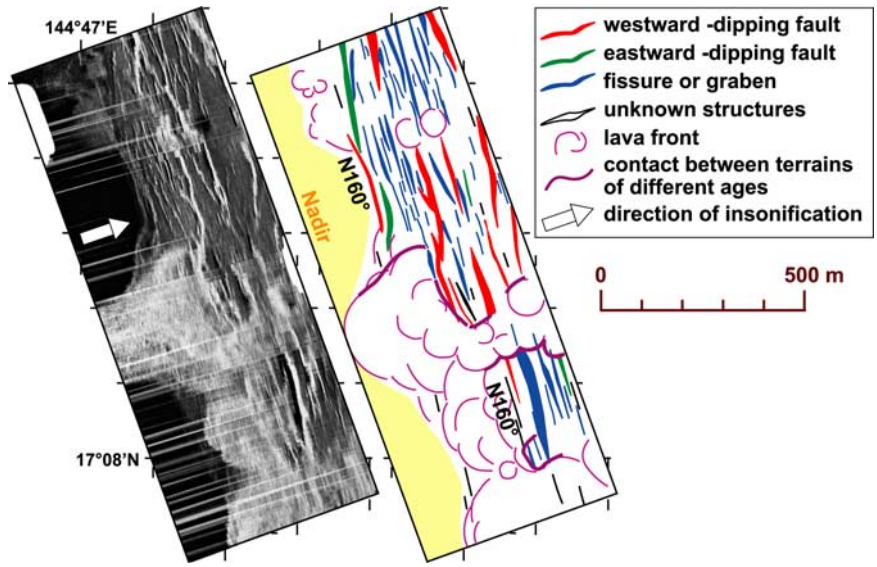

Figure 14. Small-scale side-scan mosaic with geological interpretation showing intensively fissured terrain covered by fresh flows. Almost all fractures are trending ~N160°E. Location in Figures 7 and 8.

between swaths and (2) recent lava flows may cause a single large fault to be mapped as multiple structures.

5.2. Fissure Width

[35] Fissure width could not be measured with confidence since it is often of the same order as the resolution of data. In general, fissure width is a few meters, but 10- to 20-m-wide fissures are not uncommon (Figures 12, 14, and 15). Fissure widths do not increase systematically across the survey area, as might expected if fissures were initiated at the rift axis, close to the neovolcanic zone and continue to grow in response of the far-field tectonic stresses as new crust was created and they were rafter off-axis. According to *Wright et al.* [1995b], the absolute depth of fissure penetration (Z) is defined by the following equation:

$$Z = \frac{(G/(1-\nu))(w/2)}{\sigma},$$

where Z is the calculated depth of fissure penetration, w is the measured width of the fissure, G is the static shear modulus of the host rock, ν is Poisson ratio, and σ the stresses at the time of fissure formation. Using the same values of G, ν and σ as *Wright et al.* [1995a] and *Bohnenstiehl and Kleinrock* [2000] to measure fissure depth as the East Pacific Rise and at Mid-Atlantic Ridge rift valley, respectively, we find that most of the fissures (less than 4–5 m in width) do not exceed 500 m in depth below the seafloor. The widest fissures (~20 m wide) could reach a depth of nearly 2 km beneath the seafloor. However, provided the applied tensile stress increases with depth, *Nur* [1982] concluded that the length of the cracks should usually be equal to or greater than their depths. According to that statement, cracks in our survey area should not exceed ~1.3 km in depth since their length do not exceed 1250 m.

5.3. Fracture Orientation and Distribution

[36] The strike of lineaments was taken as the azimuth of the line joining the endpoints of each of them. Fractures orientations are quite variable, with a mean strike of N163.8°E, that is, roughly equal to the mean strike measured for large (>5-km-long) faults mapped on surface bathymetric data close to the segment midpoint. Most of the fractures (~76% of the whole population) trend ~N160°E (i.e., parallel to the ridge axis at the segment center), but there is a prominent set of fractures (~24%) trending ~N175°E (~15° clockwise of the local trend of the ridge axis, and ~5° counterclockwise of the local trend of western bounding fault of the rift valley) (Figure 19). On the eastern side of the valley, in the vicinity of the eastern valley wall, we observe "y-type" connections (Figure 20) resulting from linkage of faults with different azimuths (~N160°E and ~N175°E). Similar connections have been described by *Dauteuil and Brun* [1996] within the axial valley of the obliquely spreading Mohns Ridge (North Atlantic).

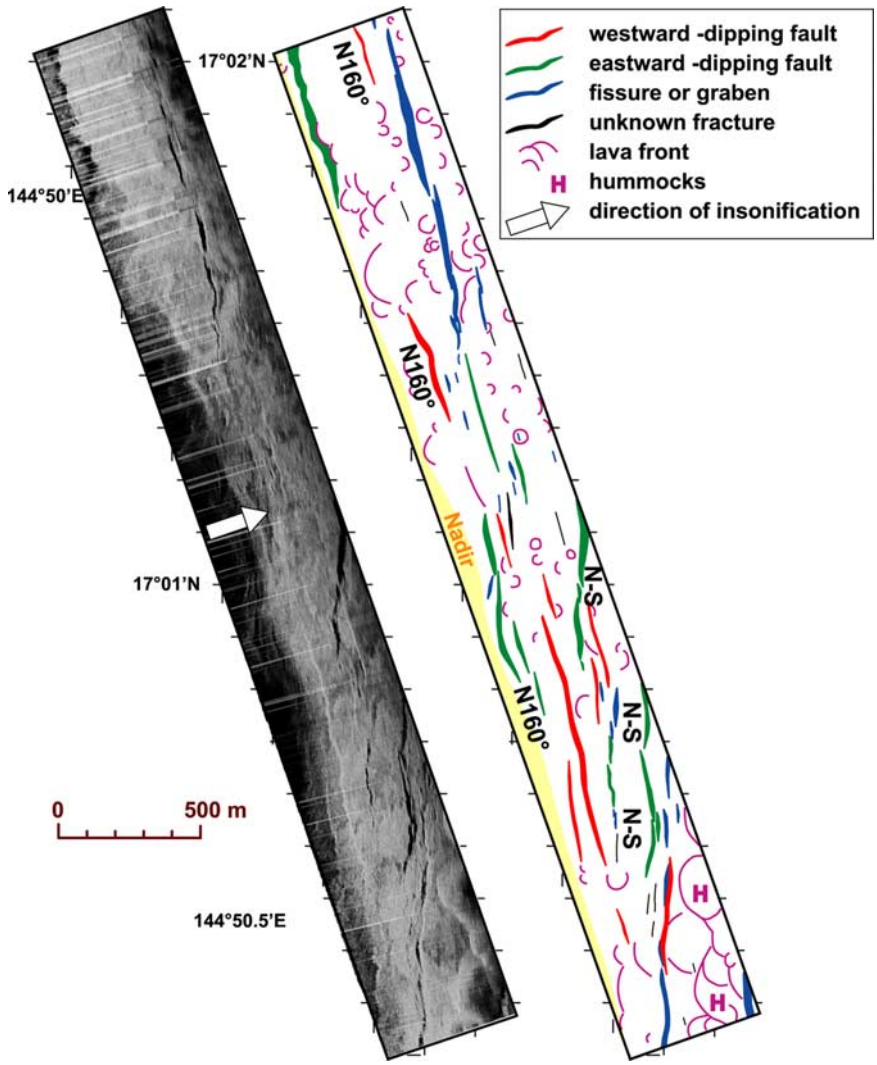

Figure 15. Side-scan mosaic with geological interpretation, showing the two distinct sets of faults described in section 5.3. Location in Figures 7 and 8.

[37] In order to analyze in more detail the orientation of fractures, we divided the study area into ten parts (five are located west of the valley axis and five to the east) (Figure 21). It appears that the N-S set of faults is absent in some boxes (boxes 1, 3, 10), clearly expressed in other (boxes 2, 4, 6, 8) and present, but at a lesser extent, in few boxes (boxes 5, 7). The set of ~N175°E faults is indeed not expressed all over the valley floor, but rather over its eastern part as far as the foot of the eastern valley wall (Figures 8 and 21). By contrast, ~N160°E trending faults are found everywhere in the survey area.

[38] Both sets of faults show the same degree of evolution: they are found within intensively faulted (i.e., relatively old) seafloor but also within relatively fresh flows. Traces of both sets of faults are sometimes curvilinear, indicating that linkage seems to have affected both sets of faults in an almost equal manner. The width of fissures and the throw of faults (roughly estimated from the width of their scarps) seem to be also relatively similar for both sets of faults.

[39] Figure 22 shows the distribution of fractures lengths (L) of ~N160°E- and ~N175°E-oriented fracture sets, plotted on log linear and log-log scales. Both sets of fractures exhibit power law distributions with values of 1.83 and 1.66 of the power law exponent C, respectively. Correlation coefficients for power law fits are 0.990 and 0.975. We also notice that ~N175°E-oriented fracture set displays a straighter curve than ~N160°E fractures on log linear plot and then tends to have a more exponential distribution. This is consistent with a

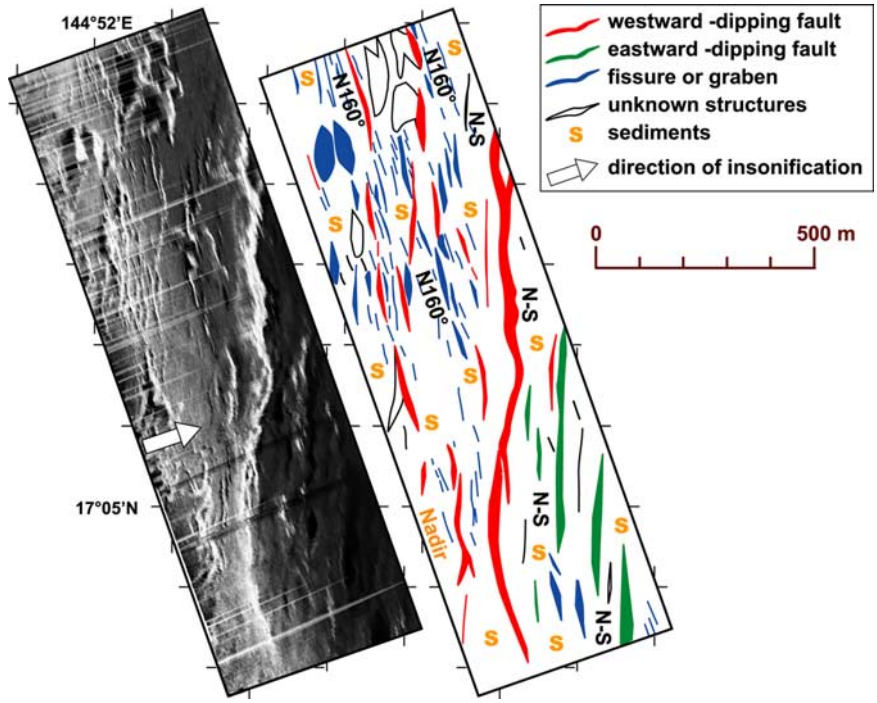

Figure 16. Small-scale side-scan mosaic with geological interpretation, showing the faulting pattern close to the ~N-S-trending eastern valley wall. Location in Figures 7 and 8.

quite good (0.969) coefficient of correlation for the exponential fit of ~N175°E fractures.

6. Discussion

6.1. Morphology of Lava Flows as a Proxy for Eruption Mechanisms

[40] No direct observations (such as dives or camera surveys) have been performed in our survey area, preventing us from being able to distinguish between different lava flows. By comparison with other areas where similar constructional features have been mapped using similar deep-tow side-scan systems, and further explored by diving or by using camera, we can infer the nature of the flows in our survey area. Hummocks and hummocky ridges that are similar to the ones we observe have been recognized on the Mid-Atlantic Ridge (MAR) and the Southwest Indian Ridge, and camera surveys in these areas show that each hummock usually corresponds to an individual pillow flow with steep flow fronts and low relief flow tops causing the hummocky morphology [e.g., *Smith and Cann*, 1995; *Lawson et al.*, 1996]. Hummocky domes have also been mapped and explored using bottom cameras on the southern East Pacific Rise (EPR) and the Juan

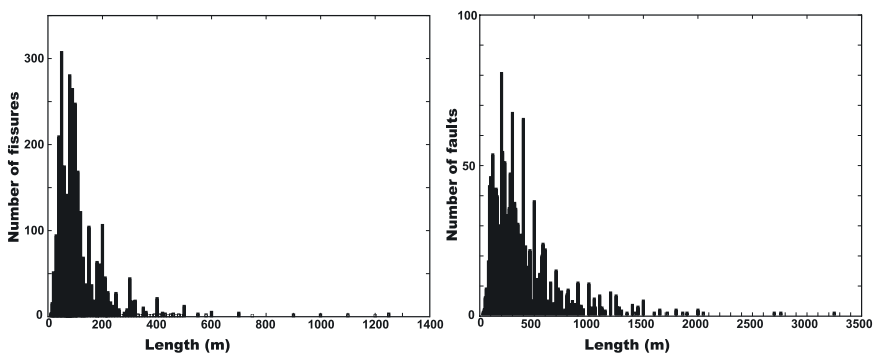

Figure 17. Length distribution of (left) 2347 fissures and (right) 1777 faults mapped on the valley floor from Wadatsumi data. The mean length is 118 m and 355 m for fissures and faults, respectively.

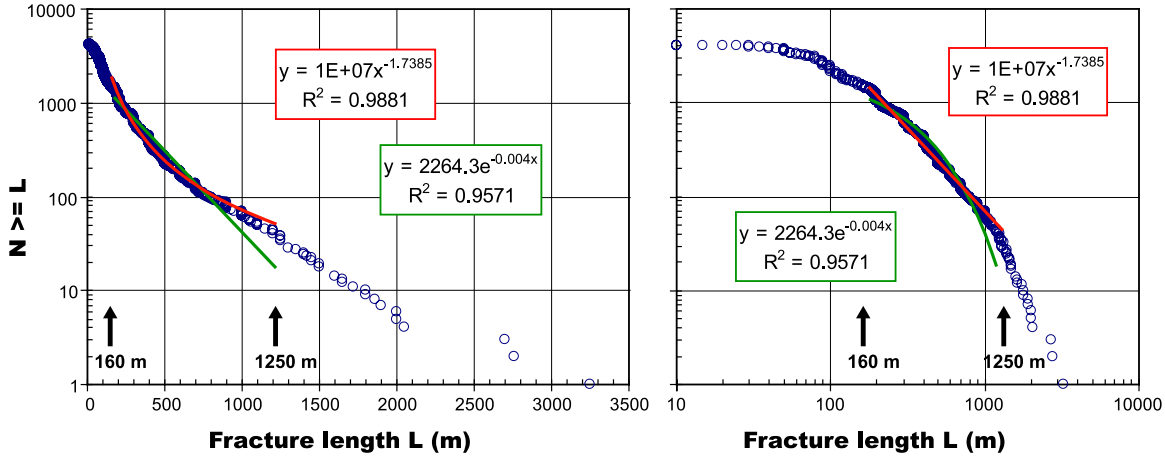

Figure 18. Cumulative frequency (N = number) plot of 4123 fractures lengths (L). (left) Log linear scale. (right) Log-log scale plot. A power law fit of the data is indicated in red. An exponential fit is indicated in green. The power law fit is the best, with an exponent of 1.74 and a correlation coefficient of 0.99. Curve fits are determined only through the population of faults between 160 and 1250 m in length.

de Fuca Ridge (JdF): they appear to be formed of pillow lava, with minor lobate lava flows [e.g., *White et al.*, 2000; *Chadwick and Embley*, 1994]. At the EPR and JdF, smooth flows correspond to sheet or lobate flows [e.g., *Embley and Chadwick*, 1994; *Perfit and Chadwick*, 1998] and at the Serocki volcano (MAR), they are formed by pillows [*Bryan et al.*, 1994]. The smooth lava flows with a short (~50–100 m) wavelength undulating surface we mapped between 16°55.5′N and 17°03′N (i.e., in the vicinity of the segment midpoint) could thus be formed by pillow flows. It seems to be confirmed by the observation of small-size hummocks emerging among smooth flows, few kilometers more to the north.

[41] Lava effusion rate exerts a strong control on lava flow morphology in the submarine setting: low effusion rate eruptions produce hummocky flows and high effusion rates rather produce smooth lava flows [e.g., *Ballard et al.*, 1979; *Griffiths and Fink*, 1992; *Gregg and Fink*, 1995]. Magmatic overpressure in the Axial Magma Chamber (AMC) is likely to control the effusion rate [e.g., *Rubin*, 1995; *Head et al.*, 1996]. *White et al.* [2002] calculated that a variation in the

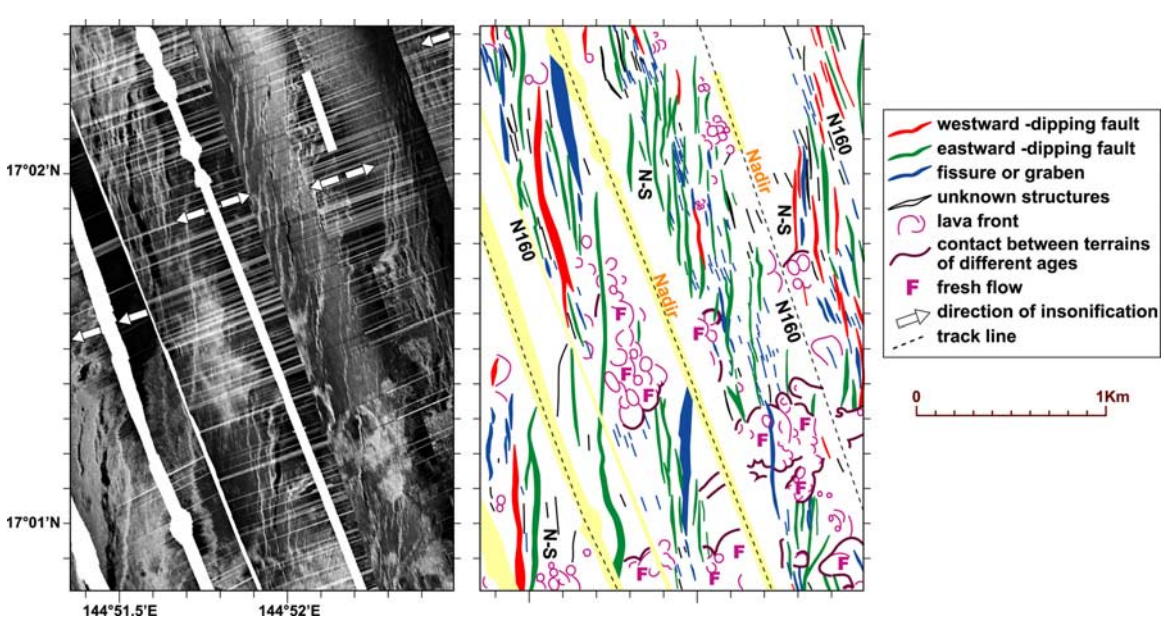

Figure 19. Small-scale side-scan mosaic with geological interpretation, showing numerous ~N-S fissures and faults. Location in Figures 7 and 8.

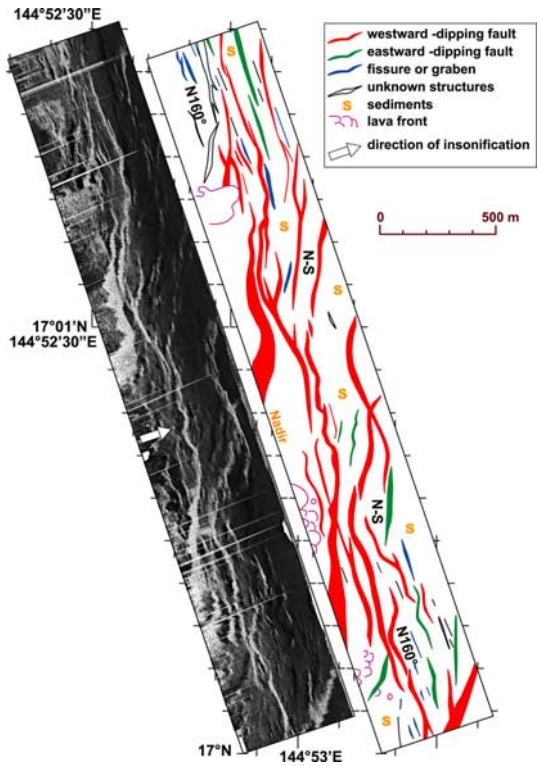

Figure 20. Small-scale side-scan mosaic with geological interpretation, showing breached relay ramps and abandoned splays. Location in Figures 7 and 8.

depth of the AMC by ~100 m could change the magma pressure by ~0.1 MPa in a 1-m-wide dike. The possible deepening of the AMC depth documented by surface bathymetric and gravity data in our study area, or even its disappearance toward the segment end, could lead to a dramatic decrease of the effusion rate toward the segment end. *Gregg and Fink* [1995] also suggest that slope variations may control the lava morphology: steep slopes would make flows travel at high speed and then likely host smoother flows than lava flowing on gentle slopes. In our case, slope appears not to play such a major role in along-axis lava morphology variation because lava domes form on the steepest (4–10°) slopes, and smooth lava ponds on less than 4°-steep slopes. Cooling rate and lava viscosity, which is related to the temperature and chemical composition of the magma, also influence lava morphology [e.g., *Bonatti and Harrison*, 1988; *Gregg et al.*, 1996].

6.2. Volcanic Plumbing System

[42] Within the median valley floor itself, the largest fissures and faults appear to be insufficient in size to intersect a primary magma source at depth. From this, we suggest that lava flows at this location formed above dikes ascending to the surface vertically or through a combination of vertical and lateral propagation, as suggested by authors for other rift zones [e.g., *Head et al.*, 1996]. However, the large amount of fresh lava flows along the western wall of the axial valley imaged by deep-tow sonar may suggest that this bounding fault may have been used as conduit for magma delivery to the surface. This hypothesis would be consistent with observations of gabbro bodies within mantle rock shear zones in ophiolites [e.g., *Allerton and MacLeod*, 1998].

[43] Along-axis changes in magma morphology suggest that the volcanic plumbing system varies on a 10- to 15-km scale. One possibility is that long dikes propagate upward and along-axis from segment center toward its end. Low-effusion eruptions tend to occur near the segment end, at the vicinity of the propagating tip where the dike is the narrowest and the magma has traveled the farthest. Such a mechanism of magma travel and eruption has been proposed by *Embley and Chadwick* [1994] (JdF), *White et al.* [2002] (EPR), and *Smith and Cann* [1999] (MAR). It is consistent with the observation of earthquakes swarms associated with dike propagation over tens of kilometers along ridge axes [e.g., *Dziak et al.*, 1995; *Fox and Dziak*, 1996]. *Embley and Chadwick* [1994] proposed that aligned vents separated by up to 1 km can be related to a single feeder: lava is erupted each time the dike intersects the seafloor during its propagation, as observed on subaerial rift zones [e.g., *Richter et al.*, 1970; *Swanson et al.*, 1976; *Delaney and Pollard*, 1982]. Another possibility is that eruptions near segment ends occur from short, narrow dikes above smaller and cooler magma sources. The resulting lower magma driving pressures and higher magma viscosities would lead to low-effusion rate eruptions [*White et al.*, 2002].

[44] The hummocky domes form linear arrays with individual domes spaced up to 600 m apart in our study area. From this, we infer that they formed above the same dike. Hummocky ridges also likely formed above dikes that have reached the surface [e.g., *Head et al.*, 1996; *Smith et al.*, 1995; *Smith and Cann*, 1999]. Along the 17°N segment, the length and the trend of the hummocky volcanic features (whether ridges or aligned mounds) indicates that dikes propagated over at least 9 km in directions ~N160°E and ~N-S. We also infer that smooth flows and the small hummocky ridge observed around 17°N/144°51′E

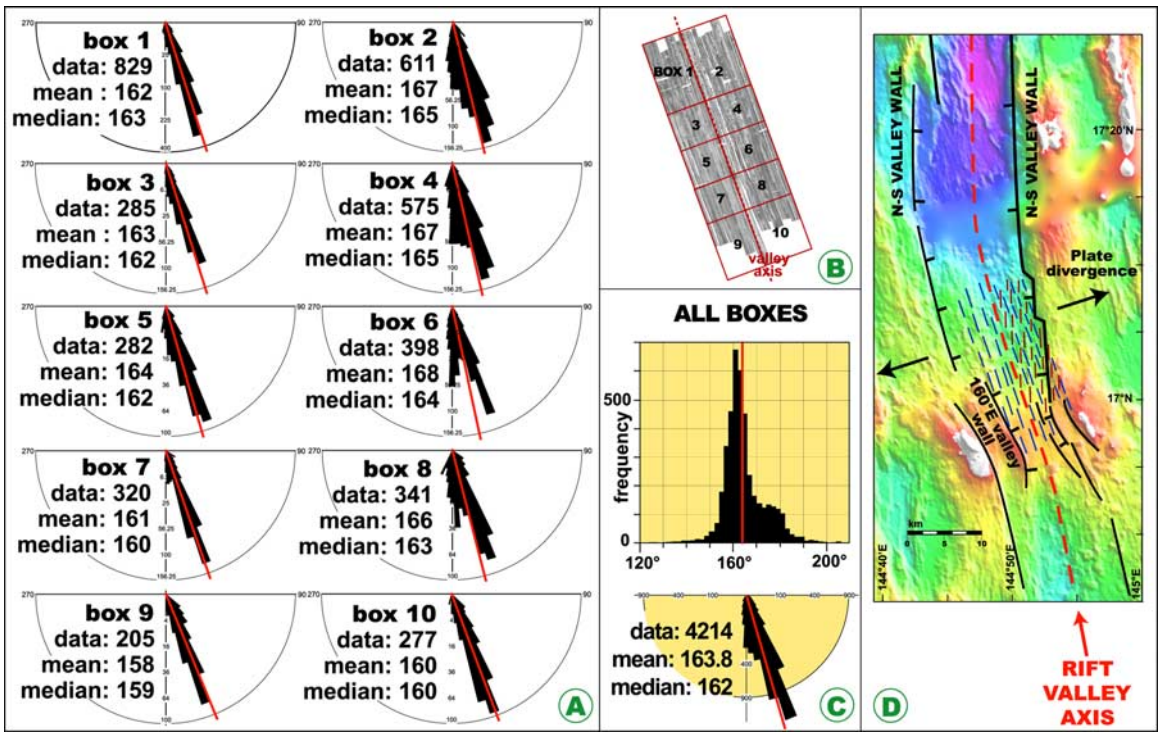

Figure 21. (a) Rose diagrams showing the strike of fractures of the rift valley for the 10 subareas indicated in Figure 21b. For each box, the total number of fractures and the mean and the median value of the population are indicated (in degrees). The mean value is also represented as a red line on each rose diagram. (c) Frequency histogram and rose diagram for the whole fracture population. (d) Simplified map of the location of the ~N160°E and ~N175°E sets of fractures within the axial valley of the 17°N segment.

(Figure 11) formed during a single eruptive event. It is indeed commonly observed during dike-fed fissure eruptions on land, that soon after an eruption begins along a "curtain of fire" located above a dike, most of the fissure system shuts down, the flow of magma localizes, and lava is discharged from a few discrete vents for the remainder of the eruption with a lower effusion rate [e.g., *Richter et al.*, 1970; *Swanson et al.*, 1979; *Delaney and Pollard*, 1982; *Peterson et al.*, 1994; *Head et al.*, 1996]. Similarly, at the 17°N segment center, we suggest that an early stage of eruption produced smooth lava flows, which then localized into a 500-m-wide and 2.5-km-long

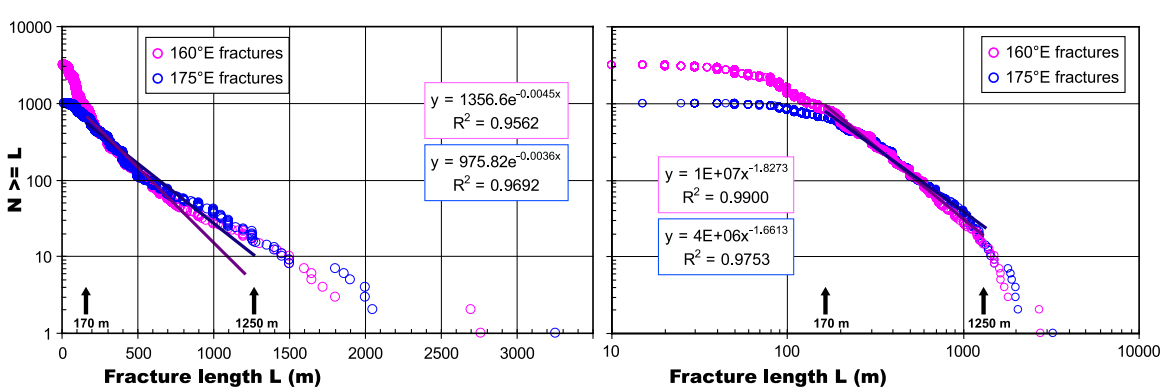

Figure 22. Cumulative frequency (N = number) plot of ~N160°E (in pink) and ~N175°E (in blue), 170- to 1250-m-long fracture lengths (L). (left) Log linear scale with exponential fit for both populations. (right) Log-log scale plot with power law fit for both populations. The power law fit is generally the best, with an exponent of 1.83 and 1.66 for ~N160°E and ~N175°E fractures.

(minimum) hummocky ridge as effusion rate decreased.

6.3. Asymmetry of the Spreading

[45] The region of highest reflectivity observed from surface backscatter data on the eastern side of the valley, south of the segment midpoint (Figure 5c) likely represents the most recent locus of volcanism and is also associated with a strong magnetization peak. From this, we suggest that this area represents the location of the new spreading axis that has recently jumped ~10 km east, from 144°53′E to 144°58′E. Asymmetric spreading may thus occur through discrete eastward ridge jumps, as proposed by *Deschamps and Fujiwara* [2003] for other segments of the Mariana spreading ridge. Such an eastward ridge jump is however only visible in the southern half of the segment. The northern half shows indeed a single high backscatter area coincident with the axial valley (Figure 5c). This might indicate that ridge jump is not occurring exactly at the same time along the whole spreading segment. It might start at a location where the lithosphere is hottest and thinnest.

[46] The contrast shown by deep-tow data between fresh-looking volcanic terrain on the western side of the valley, and intensely faulted seafloor covering the eastern side (section 4.3) does not necessarily indicate asymmetric accretion at the segment scale. The fact that the fresh-looking volcanic terrain is associated with a negative peak of the positive magnetization (Figure 5a) suggests that volcanism is not a steady state feature at that location. Our data are then insufficient to confirm the hypothesis of *Allerton et al.* [2000] that asymmetric spreading is occurring through the addition of new crust only on the fastest side of the valley.

6.4. Factor Controlling Faults and Dikes Direction and Distribution

[47] From surface data, the overall trend of the rift valley is ~N175°E. The longest abyssal hills outside the rift valley and especially at the eastern side of the valley show similar orientations (Figure 2). However, at the segment magmatic center, the local trend of the rift valley is ~N160°E, almost perpendicular to the ~N73°E direction of opening predicted from geodetic observations [*Kato et al.*, 2003]. Deep-tow side-scan sonar data indicate that the most prominent lineaments within the rift valley have ~N160°E and ~N175°E trends. ~N160°E lineaments are ubiquitous and the most abundant in the survey area and they parallel the local trend of the rift valley at segment center. ~N175°E fractures are preferentially located on the east of the valley axis as far as its eastern wall that consists of en echelon N-S normal faults.

[48] We suggest that ~N160°E-oriented small fractures and large faults are formed in response to the regional stress field associated with ~N73°E-directed plate separation and that large N-S faults and abyssal hills outside the rift valley developed within an earlier ~E-W stage of plate separation. This implies that the orientation of the regional stress field varied from ~E-W to ~N73°E about one million years ago, as shown by the trend of abyssal hills outside the valley and the crustal ages provided by the magnetic data. Only the most magmatic part of the segment, where the lithosphere is the thinnest and the hottest and support relatively small faults, can respond quickly to this regional stress field change, through the emplacement of ~N160°E directed dikes and the initiation and development of parallel fissures and faults. Toward the segment ends, the thicker and colder lithosphere supports much larger and steady state rift bounding faults, which would have a delay in responding to a change of the regional stress pattern. Large faults such as the ~N-S-trending one that bounds the northeastern side of the valley have not yet reoriented.

[49] According to this scenario, the formation of ~N175°E obliquely oriented small-scale fissures and faults, as well as the emplacement of few N-S hummocky ridges require that the local least compressive stress direction deviate by ~15° from that predicted by the present regional stress field associated with ~N73°E-directed plate separation. We hypothesize that this local stress field reorientation is triggered by the reactivation of the large (53-km-long, up to 2-km-high), ~N-S-trending normal fault that bounds the eastern side of the rift valley from ~17°28′N (close to the RTI) to ~16°59′N (almost at the segment center). ~N175°E-trending lineaments and ~N-S hummocky ridges are found only on the eastern part of the rift valley in the vicinity of this fault.

[50] We performed a series of 3-D boundary element calculations to investigate the effects of a large rift-bounding normal fault trending oblique to the regional stress field associated with plate separation, on the stress state and fracture development at the adjacent rift valley. We modeled the stress field near such a fault using the 3d-def program [*Gomberg and Ellis*, 1994]. The fault is

modeled as a stress-free plane embedded in homogeneous elastic half-space. The total stress on each fault patch is the sum of the remote stress and the stress due to slip on each fault patch. The latter is estimated using the *Okada* [1992] solutions assuming that slip is uniform but arbitrary on each fault patch and opening of the fault surface is forbidden. The numerical code 3d-def inverts for the slip distribution that results in zero shear stress on the fault. Figure 23 shows the pattern of stress orientation and magnitude at the surface that is produced by this slip distribution. As long as the constitutive behavior is elastic, the stress pattern does not depend on the amplitude of remote stress. By contrast, the amplitude of slip and therefore local stresses scales linearly with the remote stress and Young's modulus. The only variables are the geometry of the predefined fault surfaces with respect to the direction of remote extension. In the model, the fault has a length of 100 km (making it effectively semi-infinite), a dip of 55° degrees toward the west, and a depth that varies from 5 km to the north to 0 km to the south (with the taper of the fault being defined by an semi-elliptical shape and extending over 14 km). Such an along-strike variation of the dimension of the fault is indeed suggested by surface data. The fault surface is discretized into ~700 elements, each a 1×1 km square. We determine the slip magnitude and direction on each of these elements required to obtain a stress-free surface. The inferred slip distribution is nonuniform, being maximum at the surface at the center of the fault and tending to 0 at the edges of the fault. Finally we determined the stress field at the seafloor produced by N70°E-directed regional extension and modeled fault motion.

[51] Figure 23a shows the direction along which fractures will preferentially nucleate (i.e., the direction perpendicular to the calculated least principal stress σ_3) if only the N-S fault is active. In the axial valley, far from the fault, fractures nucleate along a ~N160°E direction, perpendicular to the regional stress field. Closer to the fault, where the hanging wall is bending due to the displacement along the fault, σ_3 is rotated clockwise by ~15°, so that it trends roughly perpendicular to the fault plane. The model predicts that at the location of maximum σ_3 (dashed line in Figure 23), ~N173°E fractures will develop above the normal fault plane all along the fault. These fractures would result from the bending zone associated with and parallel to the main ~N-S fault. As the depth of the fault decreases southward, the bending area (i.e., the location where ~N173°E fractures likely nucleate) narrows and becomes closer to the fault. At the southern tip of the fault, the location of maximum σ_3 is no longer related to the bending area: the model predicts that only ~N160°E fractures will nucleate.

[52] Figure 23b shows a similar model but with an additional antithetic fault that represents the western wall of the axial valley, from RTI to the north as far as its midpoint to the south. As observed on surface data, the easternmost bounding fault trends ~N-S but the westernmost one (2.8 km deep) trends ~N160°E (Figure 2). This model indicates that the bulge area associated with the westernmost fault influences the location of the bulge associated with the ~N-S fault. The result is that ~N160°E-oriented fractures are expected in the western part of the valley close to the ~N160°E rift western bounding wall, ~N175°E fractures are favored in the vicinity of the N-S major fault as far as 15 km from its southern tip, and ~N165°E fractures form in the vicinity of the fault tips, that is, the segment midpoint. Such a pattern is in agreement with the distribution of small fractures observed in deep-tow side-scan sonar data.

[53] Our models indicate that flexure of the seafloor in the hanging wall of a large normal fault trending oblique to the regional stress field associated with plate separation counteracts the regional stress field near the fault, allowing for the development of secondary fissures and faults at an angle oblique to the ridge axis. Our models resemble analog simulations of oblique rifting, which is by definition an opening along a rift which walls trend oblique with respect to the regional stress field [e.g., *Dauteuil and Brun*, 1993, 1996; *McAllister et al.*, 1995]. These experiments show that at oblique rift margins, tensional stresses are reoriented by a secondary stress field related to a change in boundary conditions, resulting in the formation of two distinct subpopulations of faults during rifting. This reorientation of the stress field is explained by the presence of a secondary stress system localized along the flexure that develops in the clay where the latex sheet (which represents the valley floor) is joined to the metal plate (on each side of the modeled rift) [*Clifton et al.*, 2000]. A change in boundary conditions between the rift axis and its margins are also evoked to explain the presence of two sets of faults formed during oblique extension in the northern North Sea [*Faerseth et al.*, 1997]. We note that the ~N175°E-oriented fracture set may have a more exponential distribution than the ~N160°E population (Figure 22).

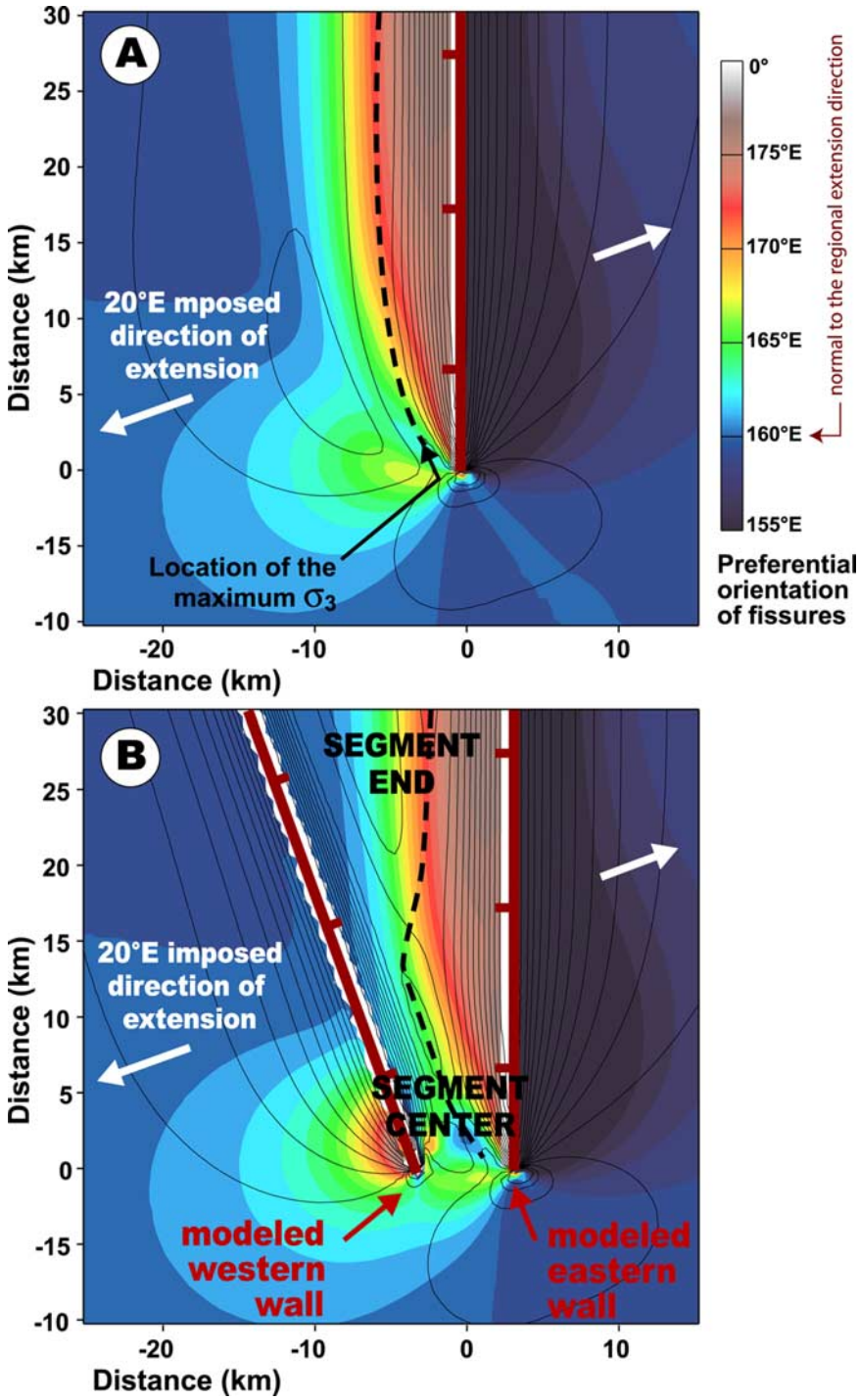

Figure 23. Results of a BEM showing the influence of preexisting major rift-valley bounding faults on the direction of the local surface stress field. The imposed direction of extension is ~N70°E. (a) In color, direction along which fractures will preferentially nucleate in the vicinity of a major ~5-km-deep, westward-dipping N-S fault trending oblique to the regional stress field associated with the plate separation. This fault represents the eastern wall of the wall from the segment midpoint (to the south) as far as the RTI (to the north). Intensity of σ_3 is shown by black contours, and its maximum is indicated by the dashed line. (b) Same calculation but with the addition of a ~2.8-km-deep, N160°E-trending, eastward-dipping fault that represents the western wall of the study area rift valley.

This might mean that ~N175°E-trending population is slightly more evolved or that the mechanisms of initiation for both sets of faults are different. Analog models performed by *Supak et al.* [2003] indeed predict an exponential distribution rather than a power law distribution of fractures associated by lithospheric flexure.

[54] We rule out the hypothesis that suggests that the oblique set of fractures and hummocky ridges in the 17°N segment is formed in an enhanced tensile stress field associated with the inflation of the Axial Magma Chamber (AMC) as was proposed for other locations [e.g., *Lawrence et al.*, 1998; *Gudmundsson*, 1998; *Koenig and Pollard*, 1998]. If it were the case, the stress-field rotation would only be temporary and would only affect fractures and volcanic products within the valley, but not the large bounding faults such as the one that bounds the northeastern side of the valley. We also suggest that the oblique set of fractures cannot result from the shear couple that is established near the RTI (Ridge-Transform Intersection) [e.g., *Karson*, 1988], because it is observed at the magmatic center of the segment, 70 km away from the RTI.

7. Summary and Conclusions

[55] Using high-resolution Wadatsumi side-scan sonar data, and surface bathymetry, reflectivity, gravity and magnetic data, we have analyzed the volcanic construction and tectonic deformation within the central part of a spreading segment of the slow-spreading Mariana Ridge. Significant along- and across-axis variations in the volcanic and deformation styles are found. Our observations support the following conclusions:

[56] 1. The rift zone is characterized by well-developed extensional structures including tension fractures, normal faults and grabens. The fracture population within the rift valley can be described by a power law with an exponent of 1.74, and did accommodate ~1.1–3.4% of tectonic strain within the inner valley floor.

[57] 2. Surface magnetic data indicates highly asymmetric spreading processes at the segment scale, the half-spreading rate being two to three times larger on the western side of the valley than on its eastern side. Such an asymmetry is also observed on two other spreading segments of the Mariana Ridge to the north by *Deschamps and Fujiwara* [2003]. We also observe an across-axis asymmetric distribution of volcanic terrain and fractures with fresh-looking volcanic textures and fewer fractures on the western side of the valley floor. This small-scale asymmetry, however, does not necessarily indicate higher strain on the eastern part of the valley vs. higher magmatic accretion on its western part as suggested by *Allerton et al.* [2000] nor correlates with the large-scale observed asymmetry. From surface backscatter data, we suggest that asymmetric spreading is accomplished through discrete (~10 km in amplitude) eastward ridge jumps.

[58] 3. The width of fissures observed within the valley floor indicate these cracks do not exceed 1.5 km in depth and are insufficient in size to intersect a primary magma source at ~4-km depth. We suggest that laterally and vertically propagating dikes are at the origin of the eruptions on the inner valley floor of 17°N spreading segment. Up to 9-km-long hummocky ridges and aligned, closely spaced hummocky domes indicate that these dikes propagated over at least 9 km along the axis. Some of the faults that bound the valley to the west may have been used as conduits for magma delivery to the surface close to the western valley wall.

[59] 4. The along-axis variation in the volcanic morphology characterized by smooth versus hummocky textures at the segment center and ends, respectively, suggests lower effusion rates toward the end of the segment than at its center. This effusion rate variation may be related to the deepening or even disappearance of the axial magma chamber toward the segment end, and hence to the eruption of magma from the vicinity of the propagating tip where the dike is the narrowest and magma has traveled the farthest.

[60] 5. We observe two distinct sets of fractures and hummocky ridges. Fractures trending ~N160°E are found everywhere within the axial valley, whereas ~N175°E-trending fractures and ~N-S hummocky ridges are found over its eastern part. Our boundary element models show that a difference in the strike of fractures and hummocky ridges within the axial valley is consistent with a ~N73°E direction of extension that is oblique with respect to the main ~N-S normal fault bounding the eastern side of the rift valley. Flexure of the hanging wall in the vicinity of such a fault would be sufficient to locally rotate the regional stress field. This will lead to the nucleation of fractures paralleling this major fault.

[61] 6. We suggest that a change in the direction of spreading occurred from ~E-W to ~N73°E about 1 Myr ago. It may have induced a reorganization of the axial tectonic and volcanic processes at the segment center, that is, the hottest and most magmatic part of the segment, whereas both ends of the segment, characterized by largest and more steady state faults, are delayed in reacting to such a kinematic change.

Acknowledgments

[62] We are grateful to captain F. Saito and crews of R/V *Kairei*, as well as engineers and technicians from Fugro Seafloor Survey Inc. (Seattle), O.R.I. (Ocean Research Institute, Univ. Tokyo), and JAMSTEC (Japan Marine Science and Technology Center) for their professional work during the cruise, especially with regard to the bad weather conditions and technical problems encountered during the use of the Wadatsumi. We thank H. Tokuyama and Y. Nakamura for their support before and during the cruise. We would also like to thank Maurice Tivey, Debbie Smith, Mark Behn, Dan Fornari, Brian Tucholke, Joe Cann, and Kyoko Okino for helpful discussions during various stages of this research, Fujio Yamamoto for his help in the processing of the data, and DelWayne Bohnenstiehl and an anonymous reader for very constructive reviews. The KR03-12 cruise was funded by both JAMSTEC and ORI. This research was supported by the Postdoctoral Scholar Program at the Woods Hole Oceanographic Institution, with funding provided by the United States Geological Survey.

References

Ackermann, R. V., and R. W. Schlische (1997), Anticlustering of small normal faults around larger faults, *Geology*, *25*, 1127–1130.

Ackermann, R. V., R. W. Schlische, and M. O. Withjack (2001), The geometric and statistical evolution of normal fault systems: An experimental study of the effects of mechanical layer thickness on scaling laws, *J. Struct. Geol.*, *23*, 1803–1819.

Allerton, S., and C. J. MacLeod (1998), Fault-controlled magma transport in the mantle lithosphere at slow-spreading ridges, in *Modern Ocean Floor Processes and the Geological Record*, edited by R. A. Mills and K. Harrison, *Geol. Soc. Spec. Publ.*, *148*, 29–42.

Allerton, S., J. Escartin, and R. C. Searle (2000), Extremely asymmetric magmatic accretion of oceanic crust at the ends of slow-spreading segments, *Geology*, *28*, 179–182.

Ballard, R. D., R. T. Holcomb, and T. H. van Andel (1979), The Galapagos Rift at 86°W, 3°N: Sheet flows, collapse pits and lava lakes of the rift, *J. Geophys. Res.*, *84*, 5407–5422.

Bibee, L. D., G. G. Shor Jr., and R. S. Lu (1980), Inter-arc spreading in the Mariana Trough, *Mar. Geol.*, *35*, 183–197.

Bohnenstiehl, D. R., and M. C. Kleinrock (1999), Faulting and fault scaling on the median valley floor of the TAG segment, 26°N on the Mid-Atlantic Ridge, *J. Geophys. Res.*, *104*, 29,351–29,364.

Bohnenstiehl, D. R., and M. C. Kleinrock (2000), Fissuring near the TAG active hydrothermal mound, 26°N on the Mid-Atlantic Ridge, *J. Volcanol. Geotherm. Res.*, *98*, 33–48.

Bonatti, E., and C. G. A. Harrison (1988), Eruption style of basalt in oceanic spreading ridges and seamounts: Effect of magma temperature and viscosity, *J. Geophys. Res.*, *93*, 2967–2980.

Bonnet, E., O. Bour, N. Odling, P. Davy, I. Main, P. Cowie, and B. Berkowitz (2001), Scaling of fracture systems in geological media, *Rev. Geophys.*, *39*(3), 347–383.

Briais, A., H. Sloan, L. M. Parson, and B. J. Murton (2000), Accretionary processes in the axial valley of the Mid-Atlantic Ridge 27°N–30°N from TOBI side-scan images, *Mar. Geophys. Res.*, *21*, 87–119.

Bryan, W. B., S. E. Humphris, G. Thompson, and J. F. Casey (1994), Comparative volcanology of small axial eruptive centers in the MARK area, *J. Geophys. Res.*, *99*, 2973–2984.

Carbotte, S. M., and K. C. Macdonald (1990), Causes of variation in fault-facing direction on the ocean floor, *Geology*, *18*, 749–752.

Carbotte, S. M., S. M. Welch, and K. C. Macdonald (1991), Spreading rates, rift propagation and fracture zone offset histories during the past 5 my on the Mid-Atlantic Ridge, 25–27°30′S and 31–34°30′S, *Mar. Geophys. Res.*, *13*, 51–80.

Chadwick, W. W., and R. W. Embley (1994), Lava flows from a mid-1980s submarine eruption on the Cleft segment, Juan de Fuca Ridge, *J. Geophys. Res.*, *99*(B3), 4761–4776.

Clifton, A. E., R. W. Schlische, M. O. Withjack, and R. V. Ackermann (2000), Influence of rift obliquity on fault-population systematics: Results of clay modeling experiments, *J. Struct. Geol.*, *22*, 1491–1509.

Cowie, P. A. (1998), A healing-reloading feedback control on the growth rate of seismogenic faults, *J. Struct. Geol.*, *20*(8), 1075–1087.

Cowie, P. A., C. Vanneste, and D. Sornette (1993), Statistical physics model for the spatiotemporal evolution of faults, *J. Geophys. Res.*, *98*, 21,809–21,821.

Cowie, P. A., A. Malinverno, W. B. F. Ryan, and M. Edwards (1994), Quantitative fault studies on the East Pacific Rise: A comparison of sonar imaging techniques, *J. Geophys. Res.*, *99*, 15,205–15,218.

Cowie, P. A., D. Sornette, and C. Vanneste (1995), Multifractal scaling properties of a growing fault population, *Geophys. J. Int.*, *122*, 457–469.

Dauteuil, O., and J.-P. Brun (1993), Oblique rifting in a slow-spreading ridge, *Nature*, *361*, 145–148.

Dauteuil, O., and J.-P. Brun (1996), Deformation partitioning in a slow-spreading ridge undergoing oblique extension (Mohns ridge-Norwegian Sea), *Tectonics*, *15*, 870–884.

Delaney, P. T., and D. R. Pollard (1982), Solidification of basaltic magma during flow in a dike, *Am. J. Sci.*, *282*, 856–885.

Deschamps, A., and T. Fujiwara (2003), Asymmetric accretion along the slow-spreading Mariana Ridge, *Geochem. Geophys. Geosyst.*, *4*(10), 8622, doi:10.1029/2003GC000537.

Detrick, R. S., H. D. Needham, and V. Renard (1995), Gravity anomalies and crustal thickness variations along the Mid-Atlantic Ridge between 33°N and 40°N, *J. Geophys. Res.*, *100*, 3767–3787.

Dziak, R. P., C. G. Fox, and A. E. Schreiner (1995), The June–July 1993 seismo-acoustic event at CoAxial segment, Juan de Fuca Ridge: Evidence for a lateral dike injection, *Geophys. Res. Lett.*, *22*(2), 135–138.

Embley, R. W., and W. W. Chadwick (1994), Volcanic and hydrothermal processes associated with a recent phase of sea floor spreading at the northern Cleft segment: Juan de Fuca Ridge, *J. Geophys. Res.*, *99*, 4741–4760.

Escartin, J., G. Hirth, and B. Evans (1997), Nondilatant brittle deformation of serpentinites: Implications for Mohr-Coulomb theory and the strength of faults, *J. Geophys. Res.*, *102*, 2897–2913.

Faerseth, R. B., B.-E. Knudsen, T. Liljedahl, P. S. Midbùe, and B. Sùderstrùm (1997), Oblique rifting and sequential faulting in the Jurassic development of the northern North Sea, *J. Struct. Geol.*, *19*, 1285–1302.

Fox, C. G., and R. P. Dziak (1996), Seismo-acoustic detection of volcanic activity on the Gorda Ridge, February–March, 1996, *Eos Trans. AGU*, *77*(46), Fall Meet. Suppl., F1.

Fox, P. J., N. R. Grindlay, and K. C. Macdonald (1991), The Mid-Atlantic Ridge (31°S–34°30′S): Temporal and spatial variations of accretionary processes, *Mar. Geophys. Res.*, *13*, 1–20.

Gente, P., R. Pockalny, C. Durand, C. Deplus, M. Maia, G. Ceuleneer, C. Mevel, and C. Laverne (1995), Characteristics and evolution of the segmentation of the Mid-Atlantic Ridge between 20°N and 24°N during the last 10 Myr, *Earth Planet. Sci. Lett.*, *129*, 55–71.

Gomberg, J., and M. Ellis (1994), Topography and tectonics of the central New Madrid seismic zone: Results of numerical experiments using a three-dimensional boundary element program, *J. Geophys. Res.*, *99*, 20,299–20,310.

Gregg, T. K. P., and J. H. Fink (1995), Quantification of submarine lava flow morphology through analog experiments, *Geology*, *23*, 73–76.

Gregg, T. K., D. J. Fornari, M. R. Perfit, R. M. Haymon, and J. H. Fink (1996), Rapid emplacement of a mid-ocean ridge lava flow: The East Pacific Rise at 9°46–51N, *Earth Planet. Sci. Lett.*, *144*(3–4), E1–E7.

Griffiths, R. W., and J. A. Fink (1992), Solidification and morphology of submarine lavas: A dependence on extrusion rate, *J. Geophys. Res.*, *97*, 19,729–19,737.

Gudmundsson, A. (1998), Magma chambers modeled as cavities explain the formation of rift zone central volcanoes and their eruptive and intrusion statistics, *J. Geophys. Res.*, *103*, 7401–7412.

Gupta, A., and C. H. Scholz (2000), Brittle strain regime transition in the Afar depression: Implications for fault growth and seafloor spreading, *Geology*, *28*, 1087–1090.

Head, J. W., L. Wilson, and D. K. Smith (1996), Midocean ridge eruptive vent morphology and substructure: Evidence for dike widths, eruption rates, and evolution of eruptions and axial volcanic ridges, *J. Geophys. Res.*, *101*, 28,265–28,280.

Hussong, D. M., and S. Uyeda (1982), Tectonic processes and the history of the Mariana Arc, A synthesis of the results of Deep Sea Drilling leg 60, *Initial Rep. Deep Sea Drill. Proj.*, *60*, 909–929.

Iwamoto, H., M. Yamamoto, N. Seama, K. Kitada, T. Matsuno, Y. Nogi, T. Goto, T. Fujiwara, K. Suyehiro, and T. Yamazaki (2002), Tectonic evolution of the central Mariana Trough, *Eos Trans. AGU*, *83*(47), Fall Meet. Suppl., abstract T72A-1235.

Karson, J. A. (1988), Factors controlling the orientation of dykes in ophiolites and oceanic crust. in *Mafic Dyke Swarms*, edited by H. C. Hall and W. F. Fahrig, *Geol. Assoc. Can. Spec. Pap.*, *34*, 229–241.

Kato, T., J. Beavan, T. Matsushima, Y. Kotake, J. T. Camacho, and S. Nakao (2003), Geodetic evidence of back-arc spreading in the Mariana Trough, *Geophys. Res. Lett.*, *30*(12), 1625, doi:10.1029/2002GL016757.

Kitada, K., et al. (2002), Gravity anomaly of Mariana Trough (abstract), paper presented at NSF-IFREE MARGINS Workshop on the Izu-Bonin-Mariana Subduction System, Natl. Sci. Found., Honolulu, 8–12 Sept.

Kitada, K., T. Yamazaki, N. Seama, H. Iwamoto, T. Matsuno, T. Fujiwara, K. Okino, Y. Nogi, and K. Suyehiro (2004), The tectonic features in Mariana Trough, inferred from gravity anomalies, paper presented at Japan Earth and Planetary Science Joint Meeting, Geod. Soc. of Jpn., Chiba, Japan, 9–13 May.

Koenig, E., and D. D. Pollard (1998), Mapping and modeling of radial fracture patterns on Venus, *J. Geophys. Res.*, *103*, 15,183–15,202.

Kong, L. S. L., S. C. Solomon, and G. M. Purdy (1992), Microearthquake characteristics of a mid-ocean ridge along-axis high, *J. Geophys. Res.*, *97*, 1659–1685.

Kuo, B.-Y., and D. W. Forsyth (1988), Gravity anomalies of the ridge-transform system in the South Atlantic between 31° and 34.5°S: Upwelling centers and variations in crustal thickness, *Mar. Geophys. Res.*, *10*, 205–232.

LaTraille, S. L., and D. M. Hussong (1980), Crustal structure across the Mariana Island Arc, in *The Tectonic and Geologic Evolution of Southeast Asian Seas and Islands*, *Geophys. Monogr. Ser.*, vol. 23, edited by D. E. Hayes, pp. 209–221, AGU, Washington, D. C.

Lawrence, R. M., J. A. Karson, and S. D. Hurst (1998), Dike orientations, fault-block rotations, and the construction of slow spreading crust at 22°40′N on the Mid-Atlantic Ridge, *J. Geophys. Res.*, *103*, 663–676.

Lawson, K., R. C. Searle, J. A. Pearce, P. Browning, and P. Kempton (1996), Detailed volcanic geology of the MARNOK area, Mid-Atlantic Ridge north of Kane transform, in *Tectonic, Magmatic, Hydrothermal and Biological Segmentation of Mid-Ocean Ridges*, edited by C. MacLeod et al., *Geol. Soc. Spec. Publ.*, *118*, 61–102.

Lin, J., G. M. Parmentier, H. Schouten, J.-C. Sempéré, and C. Zervas (1990), Evidence from gravity data for focused magmatic accretion along the Mid-Atlantic Ridge, *Nature*, *344*, 627–632.

Macdonald, K. C. (1998), Linkages between faulting, volcanism, hydrothermal activity and segmentation on fast spreading centers, in *Faulting and Magmatism at Mid-Ocean Ridges*, *Geophys. Monogr. Ser.*, vol. 106, edited by R. Buck, J. A. Karson, and Y. Lagabrielle, pp. 27–58, AGU, Washington, D. C.

Macdonald, K. C., S. P. Miller, S. P. Huestis, and F. N. Spiess (1980), Three-dimensional modeling of a magnetic reversal boundary, from inversion of deep-tow measurements, *J. Geophys. Res.*, *85*, 3670–3680.

McAllister, E., J. Cann, and S. Spencer (1995), The evolution of crustal deformation in an oceanic extensional environment, *J. Struct. Geol.*, *17*, 183–199.

Newman, S., E. Stolper, and R. Stern (2000), H_2O and CO_2 in magmas from the Mariana arc and back arc systems, *Geochem. Geophys. Geosyst.*, *1*(5), doi:10.1029/1999GC000027.

Nur, A. (1982), The origin of tensile fracture lineaments, *J. Struct. Geol.*, *4*, 31–40.

Okada, Y. (1992), Internal deformation due to shear and tensile faults in a half-space, *Bull. Seismol. Soc. Am.*, *82*, 1018–1040.

Pariso, J. E., J. C. Sempéré, and C. Rommevaux (1995), Temporal and spatial variations in crustal accretion along the Mid-Atlantic Ridge (29°–31°30′N) over the last 10 m.y.: Implications from a 3-D gravity study, *J. Geophys. Res.*, *100*, 17,781–17,794.

Parker, R. L., and S. P. Huestis (1974), The inversion of magnetic anomalies in the presence of topography, *J. Geophys. Res.*, *79*, 1587–1593.

Perfit, M. R., and W. W. Chadwick Jr. (1998), Magmatism at mid-ocean ridges: Constraints from volcanological and geochemical investigations, in *Faulting and Magmatism at Mid-Ocean Ridges*, *Geophys. Monogr. Ser.*, vol. 106, edited by W. R. Buck et al., pp. 59–116, AGU, Washington, D. C.

Peterson, D. W., R. T. Holcomb, R. I. Tilling, and R. L. Christiansen (1994), Development of lava tubes in the light of observations of Mauna Ulu, Kilauea Volcano, Hawaii, *Bull. Volcanol.*, *56*, 343–360.

Pickering, G., J. M. Bull, and D. J. Sanderson (1995), Sampling power-law distributions, *Tectonophysics*, *248*, 1–20.

Prince, R. A., and D. W. Forsyth (1988), Horizontal extent of anomalously thin crust near the Vema fracture zone from the 3-D analysis of gravity anomalies, *J. Geophys. Res.*, *93*(B7), 8051–8063.

Richter, D. H., J. P. Eaton, K. J. Murata, W. U. Ault, and H. L. Krivoy (1970), Chronological narrative of the 1959–60 eruption of Kilauea Volcano, Hawaii, *U.S. Geol. Surv. Prof. Pap.*, *537-E*, 73 pp.

Rubin, A. M. (1995), Propagation of magma-filled cracks, *Annu. Rev. Earth Planet. Sci.*, *23*, 287–336.

Scheirer, D. S., D. J. Fornari, S. E. Humphris, and S. Lerner (2000), High-resolution seafloor mapping using the DSL-120 sonar system: Quantitative assessment of sidescan and phase-bathymetry data from the Lucky Strike segment of the Mid-Atlantic Ridge, *Mar. Geophys. Res.*, *21*, 121–142.

Schlische, R. W., S. S. Young, R. V. Ackermann, and A. Gupta (1996), Geometry and scaling relations of a population of very small rift-related normal faults, *Geology*, *24*(8), 683–686.

Scholz, C. H., and J. Campos (1995), On the mechanism of seismic decoupling and back arc spreading at subduction zones, *J. Geophys. Res.*, *100*, 22,103–22,115.

Scholz, C. H., N. H. Dawers, J.-J. Yu, M. A. Anders, and P. A. Cowie (1993), Fault growth and fault scaling laws: Preliminary results, *J. Geophys. Res.*, *85*, 21,951–21,961.

Seama, N., and T. Fujiwara (1993), Geomagnetic anomalies in the Mariana Trough 18°N, in *Preliminary Report of the Hakuho-Maru Cruise KH92-1*, edited by J. Segawa, pp. 70–71, Ocean Res. Inst., Univ. of Tokyo, Tokyo.

Sempéré, J. C., J. Lin, H. S. Brown, H. Schouten, and G. M. Purdy (1993), Segmentation and morphotectonic variations along a slow-spreading center: The Mid-Atlantic Ridge (24°00′N–30°40′N), *Mar. Geophys. Res.*, *15*, 153–200.

Shaw, P. R., and J. Lin (1993), Causes and consequences of variations in faulting style at the Mid-Atlantic Ridge, *J. Geophys. Res.*, *98*, 21,839–21,851.

Sinton, J. B., and D. M. Hussong (1983), Crustal structure of a Short Length Transform Fault in the Central Mariana Trough, in *The Tectonic and Geologic Evolution of Southeast Asian Seas and Islands, Part 2*, *Geophys. Monogr. Ser.*, vol. 27, edited by D. E. Hayes, pp. 236–254, AGU, Washington, D. C.

Smith, D. K., and J. R. Cann (1999), Constructing the upper crust of the Mid-Atlantic Ridge: A reinterpretation based on the Puna Ridge, Kilauea Volcano, *J. Geophys. Res.*, *104*, 25,379–25,399.

Smith, D. K., J. R. Cann, and the cruise participants of CD65 (1995), Mid-Atlantic Ridge volcanism from deep-towed side scan sonar images, 25°–29°N, *J. Volcanol. Geotherm. Res.*, *67*, 233–262.

Smith, W. H. F., and D. T. Sandwell (1997), Global seafloor topography from satellite altimetry and ship depth soundings, *Science*, *277*, 1952–1956.

Spyropoulos, C., W. J. Griffith, C. H. Scholz, and B. E. Shaw (1999), Experimental evidence for different strain regimes of crack populations in a clay model, *Geophys. Res. Lett.*, *26*, 1081–1084.

Spyropoulos, C., C. H. Scholz, and B. E. Shaw (2002), Transition regimes for growing crack populations, *Phys. Rev. E.*, *65*, 056105, doi:10.1103/PhysRevE.65.056105.

Stern, R. J., M. J. Fouch, and S. L. Klemperer (2003), An overview of the Izu-Bonin-Mariana subduction factory, in *Inside the Subduction Factory*, *Geophys. Monogr. Ser.*, vol. 138, edited by J. M. Eiler, pp. 175–222, AGU, Washington, D. C.

Supak, S. K., D. R. Bohnenstiehl, and W. R. Buck (2003), Flexing is not stretching: An analog study of flexure-induced fault growth, *Eos Trans. AGU*, *84*(46), Fall Meet. Suppl., Abstract T22B-0508.

Swanson, D. A., D. B. Jackson, R. Y. Koyanagi, and T. L. Wright (1976), The February 1969 East Rift eruption of Kilauea Volcano, Hawaii, *U.S. Geol. Surv. Prof. Pap.*, *891*, 30 pp.

Takahashi, N., S. Kodaira, A. Ito, H. Shiobara, H. Sugioka, B. Kerr, I. Vlad, S. Klemperer, Y. Kaneda, and K. Suyehiro (2003), Crustal architecture of the Mariana arc, *Eos Trans. AGU*, *84*(46), Fall Meet. Suppl., Abstract T32A-0907.

Taylor, B., A. M. Goodliffe, G. F. Moorel, A. J. Oakley, P. Fryer, and EW0202 Scientific Party (2002), Multi-channel seismic images of the Mariana Trough: EW0202 initial results, *Eos Trans. AGU*, *83*(47), Fall Meet. Suppl., Abstract T72A-1228.

Tivey, M. A., and B. E. Tucholke (1998), Magnetization of 0–29 Ma ocean crust on the Mid-Atlantic Ridge, 25°30′ to 27°10′N, *J. Geophys. Res.*, *103*, 17,807–17,826.

Tolstoy, M., A. J. Harding, and J. A. Orcutt (1993), Crustal thickness on the Mid-Atlantic Ridge—Bull's eye gravity anomalies and focused accretion, *Science*, *262*, 726–729.

Vacquier, V. (1972), Geomagnetism, in *Marine Geology*, 185 pp., Elsevier, New York.

White, S. M., K. C. Macdonald, and R. M. Haymon (2000), Basaltic lava domes, lava lakes, and volcanic segmentation of the southern East Pacific Rise, *J. Geophys. Res.*, *105*, 23,519–23,536.

White, S. M., R. M. Haymon, D. J. Fornari, M. R. Perfit, and K. C. Macdonald (2002), Correlation between volcanic and tectonic segmentation of fast-spreading ridges: Evidence from volcanic structures and lava flow morphology on the East Pacific Rise at 9°–10°N, *J. Geophys. Res.*, *107*(B8), 2173, doi:10.1029/2001JB000571.

Wolfe, C. J., G. M. Purdy, D. R. Toomey, and S. C. Solomon (1995), Microearthquake characteristics and crustal velocity structure at 29°N on the Mid-Atlantic Ridge: The architecture of a slow-spreading segment, *J. Geophys. Res.*, *100*, 24,449–24,472.

Wright, D. J., R. M. Haymon, and D. J. Fornari (1995a), Crustal fissuring and its relationship to magmatic and hydrothermal processes on the East Pacific Rise crest (9°12′ to 54′N), *J. Geophys. Res.*, *100*(B4), 6097–6120.

Wright, D. J., R. M. Haymon, and M. C. Macdonald (1995b), Breaking new ground: Estimates of cracks depth along the axial zone of the East Pacific Rise (9°12–54′N), *Earth Planet. Sci. Lett.*, *134*, 441–457.